Remote Sensing of Environment 241 (2020) 111727

Contents lists available at ScienceDirect

Remote Sensing of Environment

journal homepage: www.elsevier.com/locate/rse

Development of a nighttime shortwave radiative transfer model for remote sensing of nocturnal aerosols and fires from VIIRS

Jun Wang[a,b,*], Meng Zhou[a,b,*], Xiaoguang Xu[a,c], Sepehr Roudini[a,d], Stanley P. Sander[e], Thomas J. Pongetti[e], Steven D. Miller[f], Jeffrey S. Reid[g], Edward Hyer[g], Robert Spurr[h]

[a] Department of Chemical and Biochemical Engineering, Iowa Technology Institute, The University of Iowa, 4133 Seamans Center, Iowa City, IA 52242, USA
[b] Interdisciplinary Graduate Program in Geo-Informatics, The University of Iowa, Iowa City, IA 52242, USA
[c] Joint Center for Earth Systems Technology, University of Maryland – Baltimore County, 1000 Hilltop Circle, Baltimore, MD 21250, USA
[d] Department of Finance, The University of Iowa, Iowa City, IA 52242, USA
[e] Jet Propulsion Laboratory, California Institute of Technology, Pasadena, California 91109 USA
[f] Cooperative Institute for Research in the Atmosphere, Colorado State University, Fort Collins, CO 80523, USA
[g] Marine Meteorology Division, Naval Research Laboratory, Monterey, CA 93943, USA
[h] RT Solutions Inc., Cambridge, MA 02138, USA

Keywords:
Nighttime shortwave radiative transfer
VIIRS
Remote sensing of fires
Remote sensing of aerosols
Nocturnal

ARTICLE INFO

Edited by Menghua Wang

ABSTRACT

The launch of the Visible Infrared Imaging Radiometer Suite (VIIRS) on board the Sumo-NPP satellite in 2011 ushered in a new era of using visible light and shortwave radiation at night to characterize aerosol and fire distributions from space. In order to exploit the full range of unprecedented observational capabilities of VIIRS, we have developed a nighttime shortwave radiative transfer model capability in the UNified and Linearized Radiative Transfer Model (UNL-VRTM). This capability is based on the use of additional source functions to treat illumination from the Moon, from fires, and from artificial lights. We have applied this model to address fundamental questions associated with the VIIRS sensing of aerosol and fire at night. Detailed description of model developments and validation (either directly with surface measurements of lunar spectra or indirectly through cross validation) are presented. Our analysis reveals that: (a) when convolution with the broad-range (500–900 nm) relative spectral response (RSR) function of the VIIRS Day-Night Band (DNB) is omitted, AOD retrieval from the DNB have uncertainties up to a factor of two in conditions with low or moderate AOD (<0.5 in mid-visible); (b) using a wavelength independent spectrum for the surface illumination source can lead to an AOD bias of -10% over surfaces illuminated by light-emitting diodes and fluorescent lamps, and -30% illuminated by high-pressure sodium lamps; and (c) a DNB-equivalent narrow band for AOD retrieval over the surfaces illuminated by the three types of bulbs studied in this paper is found to be centered at 585 nm at which the look-up table can be generated for AOD retrieval from DNB. Furthermore, while uncertainty in AOD retrievals from the DNB decreases as AOD increases, fire characterization can be affected by AOD; for a smoke-scenario AOD of 2.0, the DNB and SWIR (1.6 μm) radiances can be reduced by 50% depending on the fire area fraction and temperature within VIIRS pixel. DNB is overall more sensitive to smaller and cooler fires than SWIR and can be used to retrieve AOD over bright surfaces. Finally, three-dimensional (3D) radiative transfer effects and the non-collimated nature of most artificial light sources are neglected in this 1D radiative transfer (plane-parallel) model, resulting in possibly large uncertainties (e.g., the inability to reproduce side-illumination of clouds by city lights) that should be studied in future.

---

[*] Corresponding authors at: Department of Chemical and Biochemical Engineering, Iowa Technology Institute, The University of Iowa, 4133 Seamans Center, Iowa City, IA 52242, USA.

E-mail addresses: jun-wang-1@uiowa.edu (J. Wang), meng-zhou-1@uiowa.edu (M. Zhou).

https://doi.org/10.1016/j.rse.2020.111727
Received 18 July 2019; Received in revised form 11 February 2020; Accepted 15 February 2020

1. Introduction

The Visible Infrared Imaging Radiometer Suite (VIIRS) is a unique sensor carried on the current operational fleet of environmental satellites managed by the National Oceanic and Atmospheric Administration (NOAA). VIIRS is a 22-band scanning radiometer providing nominal spatial resolution of 375 m in five imagery bands (I-bands), 750 m in the sixteen moderate-resolution bands (M-bands), and the single Day-Night band (DNB) that provides near-constant 742 m spatial resolution. VIIRS differs from its predecessors such as the Moderate Resolution Imaging Spectroradiometer (MODIS) and the Advanced Very High Resolution Radiometer (AVHRR) in several important ways: (a) the growth of pixel size from the nadir to the edge of the ground track is about a factor of 2 for I- and M-bands, a much slower rate of growth than the factor of 8–10 for MODIS, and the pixel size for DNB is nearly uniform across the swath; (b) the DNB (Lee et al., 2006; Miller et al., 2013) can measure the calibrated intensity of visible light for a range of seven orders of magnitude (from daytime reflection of solar radiation to nighttime illumination by moonlight, and even atmospheric airglow and starlight (Miller et al., 2012, 2015)); (c) measurements of shortwave radiation at wavelengths of 0.87, 1.24, 1.60, 3.70, and 4.06 μm are available at night from M bands (Elvidge et al., 2013), whereas for MODIS only the 3.96 μm fire channel is available. Considering that the VIIRS will be the primary imager on board U.S. polar-orbiting JPSS series of satellites for the next two to three decades, we in this paper lay out the theoretical foundation and develop a radiative transfer model (RTM) capability for using the VIIRS DNB and other VIIRS shortwave bands for fire and aerosol remote sensing at night.

1.1. Need for a RTM for remote sensing of aerosols at night

While substantial efforts have been made in the past two decades to retrieve AOD and other aerosol properties from ground stations, aircraft, and satellite observations (see the reviews by King et al., 1999, Kaufman et al., 2002, Kokhanovsky and Leeuw, 2009, Dubovik et al., 2019 and references therein), only a few retrievals have been made for nighttime scenarios. For example, AERONET stations rely on sun/sky photometers to measure both direct and diffuse solar radiation from which aerosol properties such as AOD, single scatter albedo (SSA), and size parameters can be retrieved (Dubovik and King, 2000; Xu and Wang, 2015; Xu et al., 2015). Only in recent years have moonlight measurements been collected by ~180 AERONET sites for the derivation of AOD at night (Barreto et al., 2013; Li et al., 2016; Giles et al., 2019). In contrast, ground-based laser systems can actively detect the aerosol backscatter and extinction profiles at night (Bian et al., 2017); however, their spatial coverage is isolated. From space, satellite instruments such as MODIS, MISR, and OMI are used to retrieve AOD and other aerosol properties, but all retrievals are daytime only. Space-based lidar systems, such as CALIPSO and CATS, do provide measurements of aerosols at night, but their narrow footprints (90 m diameter for CALIPSO and 14.38 m diameter for CATS) limit the applications to full and daily global coverage.

Although there is no *operational* algorithm current in existence to conduct nighttime AOD retrievals with true global and daily coverage, several recent studies have presented research algorithms demonstrating the promising potential for the use of artificial light sources when measuring intensity from space to derive aerosol burdens at night. Using the DMSP OLS, Zhang et al. (2008) demonstrate the potential utility of city lights to retrieve AOD over airports at night. More recently, Johnson et al. (2013) and McHardy et al. (2015) take advantage of superior sensor signal-to-noise ratio, onboard aggregation, and calibration of the DNB (Wolfe et al., 2013) to retrieve the nighttime AOD. These studies have focused on isolated areas (such as small towns and airports) that have a bright surface illumination and a high contrast with the surrounding darker areas, and no AOD mapping capability was demonstrated except in an area-mean context. These retrievals assumed that: (a) the propagation of light obeys either Beer's law of extinction or deals with single scattering only in the radiative transfer, and (b) the surface albedo is completely dark, so that the surface-aerosol reflective interaction can be neglected.

In parallel to the aforementioned studies, a few investigations have also considered the DNB's potential for mapping surface $PM_{2.5}$ air quality at the *urban* scale over the last couple years (Wang et al., 2016; Fu et al., 2018). Here, the focus of these studies has been on the derivation of surface $PM_{2.5}$ concentrations at night in urban areas from space; this enterprise can provide a crucial addition to satellite remote sensing of urban air quality, a field which has seen rapid growth in research and application over the past 15 years (Wang and Christopher, 2003; Hoff and Christopher, 2009; van Donkelaar et al., 2013; Chu et al., 2016 and references therein) but which currently relies only on daytime observation of AODs. Wang et al. (2016) illustrated the potential use of DNB measurements to monitor nighttime air quality in the city of Atlanta. Subsequently, they develop regression formulas to link surface $PM_{2.5}$ concentration with DNB radiances by considering aerosol hygroscopicity and Beer's law; the regression can predict surface $PM_{2.5}$ with a linear correlation coefficient of 0.67. This study together with other recent work (Lennartson et al., 2018) reveal the distinct diurnal cycle of the relationship between AOD and $PM_{2.5}$. Not surprisingly, nighttime aerosol studies have been drawing increasing attention from the air quality research community. For example, Fu et al. (2018) have used DNB measurements to derive monthly surface $PM_{2.5}$ over Beijing, again under the assumption that the link between DNB radiance and AOD can be interpreted through the single-scattering radiative transfer assumption.

While continuous progress is being made, AOD retrieved from DNB remains limited—being retrieved either at coarse resolution (1° × 1°) or for isolated illumination sources only (Zhang et al., 2018). Furthermore, the retrieved AOD value is specified as the band AOD for the DNB spectral range of 500–900 nm, and its comparison with the AERONET AOD at 670 nm interpolated from daytime retrievals shows a linear correlation coefficient in the range of 0.5–0.6 on average (Zhang et al., 2018). Anecdotally, the potential of DNB to map surface $PM_{2.5}$ at night at the urban scale has been demonstrated for a number of case studies, these studies have relied on the aerosol single scattering assumption to relate the observed DNB radiance to AOD and to surface $PM_{2.5}$. Clearly, there is a great deal of room for improvement, and this can be not fully realized without the development and study of a fully accurate nighttime shortwave RTM to help disentangle the signals of various sources. To give an example, it remains unclear how the atmospheric transmittance in DNB will vary when the illumination source at the surface is a light-emitting diode (LED), sodium lamp or traditional incandescent out-door bulbs. Furthermore, the 500–900 nm DNB spectral range encompasses important regions of molecular absorption (principally water vapor and oxygen). It is unknown: to what degree these absorptions will affect nighttime AOD retrieval, or indeed if there is any effective wavelength that can be used to do the retrieval in order that AODs can be reported for narrow bands.

1.2. Need for a RTM for remote sensing of fires at night

The first nighttime detection of fires via low-light visible observations from space was demonstrated in the early 1970s via the Sensor Aerospace Vehicle Electronics Package (SAP) as part of the Defense Meteorological Satellite Program (DMSP; Croft, 1973). In contrast, the first reported time that fires were observed from satellite via the infrared bands alone was shown later by Matson and Dozier (1981) with the AVHRR's channel 3b centered at 3.74 μm (e.g., mid-wave infrared, or MWIR, channel). At present, fire detection algorithms have evolved from the use of AVHRR data into the realm of more sophisticated sensors and to geostationary satellites, but fire retrievals are still more or less based on MWIR and thermal infrared (TIR) (Prins et al., 1998;

Justice et al., 2002; Giglio et al., 2003; Csiszar et al., 2013; Schroeder et al., 2014). Furthermore, the Fire Radiative Power or FRP, a variable proposed by Kaufman et al. (1998a, 1998b) based solely on the calculation of brightness temperature in the 3.9 µm channel, has been shown to be a useful proxy measure of fire intensity and fire emission (Ichoku et al., 2008). FRP estimates have been used in routine fire emission inventories such as GFED and QFED (Petrenko et al., 2012; Ichoku and Ellison, 2014) and are now routinely available from VIIRS (Giglio et al., 2016). FRP is also shown to be indicative of smoke injection height (Peterson et al., 2014) and the impacts of wind speed on fire combusion (Peterson and Wang, 2013; Peterson et al., 2013).

However, advances in remote sensing of fires over the past five to eight years have shifted the focus from using MWIR to using shorter wavelengths, thanks to the advent of shortwave infrared (SWIR) measurements at night from VIIRS (see a review in Wang et al., 2020). For example, primarily based upon VIIRS's shortwave infrared at 1.6 µm, 3.7 µm and other TIR M bands, Elvidge et al. (2013) developed a nocturnal gas flare detection algorithm to retrieve sub-pixel fire characteristics. In contrast with thermal infrared channels that are traditionally used for fire detection, DNB and SWIR channels have *some* advantages in that they are much less sensitive to estimates of the background temperature, and correspondingly more sensitive to detection of fires that are flaming in situations where fire area is small and the background temperature is low (such as over snow surfaces or high mountains, Polivka et al., 2016). Indeed, by combining the DNB, MWIR, and TIR bands from VIIRS, Polivka et al. (2016) and Wang et al. (2020) develop an algorithm that enhances the detection of cooler and smaller fires and characterize the fire phase at the same time at night. With the advent of research showing the promising potential using the DNB and SWIR bands for fire detection and characterization, the apparent need is emerging for a nighttime shortwave RTM to study fundamental questions regarding how the fire emission of water vapor and smoke particles may affect the radiative transfer of radiation emitted by fires at different wavelengths as detected by DNB and SWIR, and consequently, the FRP calculations.

1.3. Scope and structure of this study

Although the aforementioned research has demonstrated the potential of the DNB to monitor nighttime fire and aerosols, fundamental questions remain to be addressed, such as:

- o How significant is the DNB's relative spectral response (RSR) function in the RTM calculation of DNB radiance? How important is it to consider Rayleigh scattering and molecular absorption from water vapor, NO_2, and O_2 to simulate DNB radiance?
- o How much effect does the resolved spectrum of specific artificial light sources have on RTM outputs and retrieved AOD, compared with an assumption of white light or a wavelength independent (or uniform) surface light spectrum?
- o Is there any effective wavelength or wavelength interval that can be used to retrieve AOD from DNB in a manner similar to that from a narrow band?
- o To what degree can smoke particles affect the radiative transfer of shortwave radiation (including DNB, 1.6 µm, and others) that originates from fires and is measured by VIIRS?

To answer these and other questions above, there is a strong requirement for a full multiple-scattering radiative transfer model (RTM) based on both moonlight and surface-leaving visible light sources. In this regard, Cao and Bai (2014) reviewed several existing RTMs and concluded that none of them are suitable for applications to VIIRS DNB at night. The RTMs they reviewed include An Army Illumination Model (AAIM), the Light Pollution Radiative Transfer (LPTRAN) model, the MODerate resolution atmospheric TRANsmission (MODTRAN) model, the Second Simulation of a Satellite Signal in the Solar Spectrum (6S) model, and the Community RTM or CRTM. AAIM and LPTRAN are generally concerned with the surface light pollution as a function of horizontal distance from the light source (Cinzano and Falchi, 2012). In contrast, MODTRAN (Berk et al., 2014), 6S (Kotchenova and Vermote, 2007), and CRTM (Liu and Boukabara, 2014), and other RTMs (Ricchiazzi et al., 1998) are widely used in the satellite remote sensing community, but their illumination sources are limited to either the Sun or the Moon. To our knowledge, none of these models offers the option to include artificial light sources on the surface, as is needed for VIIRS DNB remote sensing for aerosols and fires.

The Unified Linearized Vector Radiative Transfer Model (UNL-VRMT) (Wang et al., 2014) is the starting point for the present work. UNL-VRMT was designed as a testbed for remote sensing of aerosol (Wang et al., 2014), and it has been used in a number of aerosol retrieval and information content analyses (Chen et al., 2017; Wang et al., 2017; Xu et al., 2018). At the heart of the model is the multiple-scattering linearized vector discrete ordinate VLIDORT radiative transfer code (Spurr, 2006; Spurr and Christi, 2019).

In this paper we have added the necessary radiative transfer functionality to the VLIDORT model by including nighttime sources for moon light and surface artificial lights. The structure of this paper is as follows. Starting in Section 2 with a brief review of the nighttime radiative transfer concept, we then introduce different ways to specify surface light sources. In Section 3, validation of the model development is carried out. In Section 4, we apply our updated UNL-VRTM to VIIRS DNB measurement, and design experiments to address the above list of questions. Section 5 summarizes the paper. It should be noted that, this paper is the first installment of a two-part series study of night time RTM development and nocturnal aerosol retrieval. The impact of moonlight on VIIRS DNB AOD retrievals over the areas illuminated by artifical lights will be the main topic of subject of the second paper.

2. Nighttime RTM development

The concept of nighttime radiative transfer is illustrated in Fig. 1a. Unlike daytime periods when the Sun is the dominant light source, visible light at night primarily consists of the moonlight and artificial light. The nocturnal propagation of moonlight at night is similar to that of the sun light in the daytime. Downwelling moonlight from top-of-atmosphere (TOA) is scattered and absorbed by the atmosphere and reflected by the surface. Light that has been reflected by the surface can interact with the atmosphere multiple times before either exiting back to space or being absorbed. Light emitted by artificial lights often propagates both upward and downward (despite shielding practices to reduce the effect of light domes). The direct upward and reflected downward components interact with atmosphere through multiple scattering before reaching the satellite. Thus, the satellite signal is the results of the interaction of multiple factors, including different types of light sources, surface, aerosol, trace gas and other atmospheric components.

The following factors comprise the basic elements for a nighttime radiative scenario, and they need to be considered in the extension of UNL-VRTM for nighttime remote sensing applications. Specifically,

(1) *Lunar irradiance*. As the moon is only a reflecting body, the lunar irradiance depends strongly upon its spectral surface albedo. Its signal at the top of Earth's atmosphere is much weaker (by a factor of 10^6) than the solar irradiance. The Sun-Earth-Moon geometry, that determines the distance of the propagation of the light and the moon phase, also effects the lunar irradiance by varying the effective size (in terms of solid angle) of the reflector. The most significant factor in the variation of moonlight is the lunar phase, which determines the fractional illumination of the lunar disk as seen from Earth. Although in general, the Earth-moon distance and the moon phase follow approximately a 28 days cycle, there remain non-negligible differences of these parameters among each cycle,

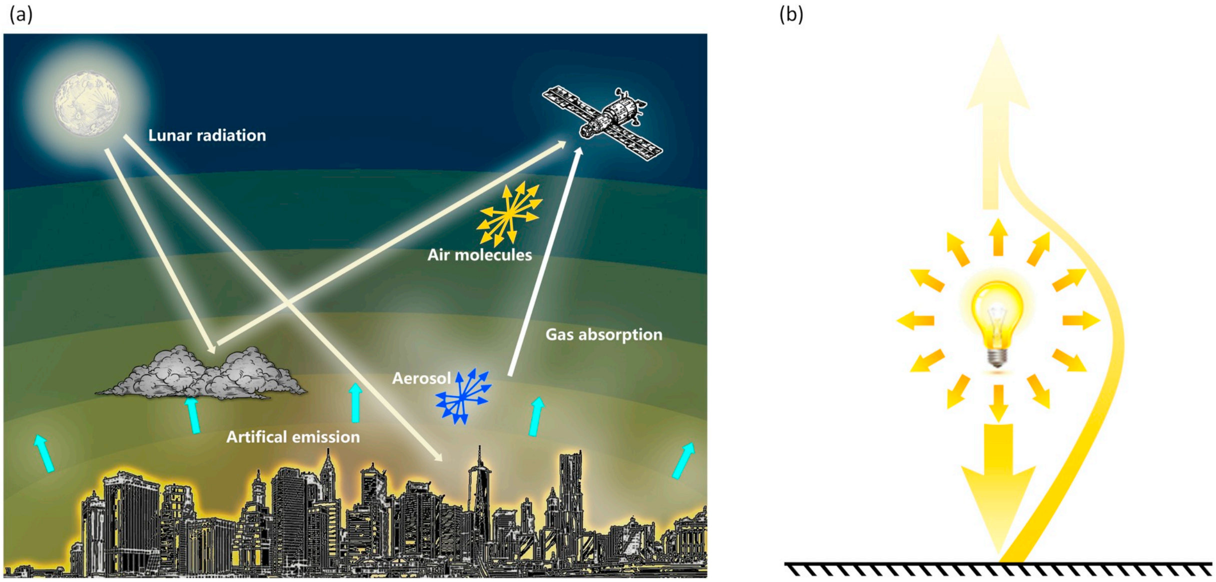

Fig. 1. (a) Key components of nighttime radiative transfer in cloud-free conditions. (b) Representation of surface bulb illumination and its interaction with surface in the model development. Please see text for details.

since both the Sun and Earth perturbs the Moon's motion significantly. Thus, an accurate modeling of the lunar irradiance is one of the fundamental requirements of the nighttime RTM.

(2) *Surface light sources*. Surface light can arise from multiple sources with distinct emission characteristics, and there are no clearly defined methods to model it. For example, light intensity from a wild fire may obey the Planck's function distribution to the first order, but artificial light emission from various lamps may follow other more energy-efficient mechanisms (e.g., sodium lamps). A more complex but realistic scenario for surface light is to regard it as a combination of the different light sources, with specific locations processing unique light emission profiles. The nighttime RTM should also have the ability to simulate the light transfer of different light spectral shapes.

(3) *Light source interactions*. The surface type and optical composition of the atmosphere (such as trace gases and aerosols) affect the light propagation in different ways. For example, a Lambertian surface may reflect the light isotropically, though in a more realistic case the surface reflectance may be anisotropic. On the other hand, atmosphere gas species will absorb light in certain bands, while strongly scattering aerosols may scatter the light and make the ground brighter. While these factors (multiple scattering, surface albedo, upward and downward factors, etc.) are important for both daytime and nighttime RTM, the nighttime RTM should also consider that the interaction of surface with the source of illumination that is near the surface (Fig. 1b). Such interaction depends on three-dimension distribution of buildings and canopy, which pose a challenging to model.

2.1. UNL-VRTM

To simplify the complexity in simulation of nighttime shortwave radiative transfer, we start the model development by first building upon our past work that combines UNL-VRTM (Wang et al., 2014) with non-linear optimal estimation theory (Rodgers, 2000). The UNL-VRTM comprises seven modules: (1) a vector linearized radiative transfer model (VLIDORT, (Spurr and Christi, 2019)), (2) a linearized Mie scattering code (Spurr et al., 2012), (3) a linearized T-matrix electromagnetic scattering code (Spurr et al., 2012), (4) a surface bi-directional reflectance distribution function (BRDF) and bi-directional polarization function (BPDF) module, (5) a module that computes Rayleigh scattering and gas absorption (with HITRAN and other molecular absorption cross section databases), (6–7) two modules for the analysis, an optimal inversion code and a visualization tool for diagnosis, respectively. Modules 1–5 encompass the forward calculations of aerosol single scattering, gas absorption, and radiative transfer, and together they constitute the foundation of UNL-VRTM. UNL-VRTM has been used in our past work for aerosol information content analysis for different designs of satellite mission concept and retrieval algorithms (Ding et al., 2016; Hou et al., 2016; Hou et al., 2017), for polarimetric algorithm development for AERONET (Xu and Wang, 2015; Xu et al., 2015), and for aerosol layer height retrieval from EPIC/DSCOVR (Xu et al., 2017). UNL-VRTM is well documented and has been used by a dozen research teams around the world (https://unl-vrtm.org).

Input profiles for UNL VRTM include atmospheric properties and constituents (e.g., temperature, pressure, aerosol mass concentration or layer AOD, water vapor amount and other trace gas volume mixing ratio profiles), microphysical aerosol parameters themselves (e.g., size distribution and refractive index), and surface parameters (such as reflectance, temperature, and surface-leaving radiances). The UNL-VRTM is designed to deliver radiative calculations for an atmospheric column that has two or more modes of aerosols, typically one fine-mode and one coarse-mode aerosol. Outputs of the UNL-VRTM include four Stokes 4-vectors for polarized light at user-defined wavelengths, as well as the sensitivities (Jacobians) of Stokes-vector components with respect to aerosol particle microphysical and optical properties in each model layer and the column-integrated parameters, including those regulating aerosol single scattering properties (e.g., aerosol size distribution, refractive index, and particle shape) for each aerosol mode, and the information content of the synthetic data (expressed as Degree of Freedom for Signal or DFS values for these physical parameters).

2.2. New development for including the lunar source

We have added to the UNL-VRTM a spectrally-resolved moon-phase based lunar irradiance model developed by Miller and Turner (2009). The spectral resolution of this dataset is 1 nm, with a spectrum range from 202 to 2800 nm. While this data package by Miller and Turner (2009) does include results computed for any given day and hour up to the year 2100, its size is very large. To reduce memory storage, we have incorporated an additional module to compute the lunar phase angle of any given day into UNL-VRTM; this module is not part of the package provided by Miller and Turner (2009) and it takes as input the time and geographical coordinates of the observer in order to compute the corresponding geometrical configurations (zenith and azimuth angles as well as the moon phase angle, earth-moon distance, and sun-moon distance), all with an error of <2 arc minutes (Schlyter, 2010). Although, the datasets compiled by Miller and Turner (2009) are comprehensive, they have several limitations, including the inability to account for temporal variations of the solar spectrum and libration effects on the lunar surface albedo. The overall uncertainty of this database is in the range of 5%–10% (Miller and Turner, 2009).

With this new development, the spectrally resolved lunar irradiance at the top of atmosphere (TOA) can be computed for any given time and location in our planet, with explicit treatment of moon phase, earth-moon distance, and sun-moon distance. Once the downward lunar radiance at the TOA is known, its transfer in the atmosphere and its interaction with Earth surfaces are treated in the similar manner as for the shortwave radiative transfer at daytime in UNL-VRTM. Here, the moonlight is assumed to reach the TOA as a collimated beam. This assumption is based on two considerations. First, when viewed from the Earth, the solid angle of moon is indeed comparable to that of the Sun, which in part explains the existence of “perfect” solar eclipses. Thus, as with solar radiation that is emitted by the Sun in all directions and is treated as a collimated beam when it is viewed from a small solid angle, the moonlight, although a result of reflection by the moon surface to all directions, can also be approximated as a collimated and directional source when it reaches TOA. For example, for an area of 1×1 km^2 at the Earth's surface, the moonlight reaching this area is confined to a solid angle of $\sim 7 \times 10^{-12}$ sr from the moon, which is much smaller than the value of 10^{-6} sr that is normally regarded as acceptable for a laser beam to be treated as collimated beam. Secondly, by comparing the measured polarization patterns of the moonlit night sky with those of the sunlit day sky, Gál et al. (2001) showed that the polarization characteristics of a moonlit night sky are practically identical with those of a sunlit sky if the position of the Moon in the firmament is the same as that of the Sun; this suggests that the lunar source of shortwave radiation can be treated in the similar way as is done for the solar source in UNL-VRTM.

While moonlight can be treated as a collimated beam of electromagnetic plane waves as is done for direct-sun shortwave radiation (as far as atmospheric radiative is concerned), moonlight polarization properties are somewhat different. Radiation directly from the Sun is unpolarized before it reaches the TOA, while moonlight has a small degree of linear polarization (DOLP) that varies with the moon phase angle and wavelength (Pellicori, 1971). The DOLP of moonlight is nearly zero at full moon (regardless of wavelength) and can be 5–20% for wavelengths in the UV (0.34 μm) to the green part of the visible spectrum (0.51 μm) when the moon phase angle is 100°–120°; the longer the wavelength, the smaller is the DOLP. Since the DOLP of moonlight is small (up to 5% at 500 nm and generally close to zero) for the DNB wavelengths (700–900 nm), it has been neglected in our current version of UNL-VRTM. The treatment of moonlight polarization in UNL-VRTM is planned for future studies, pending more accurate knowledge.

2.3. New development for fire and artificial illumination sources

As with several other one-dimensional RTMs used in optical remote sensing for aerosols and fires (Ricchiazzi et al., 1998), UNL-VRTM does not consider the radiation interaction with the detailed canopy or building structures at the surface, and hence, upwelling radiances as the result of such interaction are treated effectively in UNL-VRTM as emitted radiances from a planar boundary (e.g. the bottom level of the model). In practice, these emitted radiances are treated as additional source terms in the equations for the thermal infrared radiative transfer (with atmospheric scattering considered). The 1-D vector RTE for plane-parallel scattering in a single layer in UNL-VRTM follows Spurr and Christi (2019):

$$\mu \frac{\partial \mathbf{I}(x,\mu,\phi)}{\partial x} = -\mathbf{I}(x,\mu,\phi) + \mathbf{S}(x,\mu,\phi) \tag{1}$$

$$\mathbf{S}(x,\mu,\phi) = \frac{\omega(x)}{4\pi} \int_0^{2\pi} \int_{-1}^{1} \mathbf{P}(x,\mu,\mu',\phi')\mathbf{I}(x,\mu',\phi')d\mu' d\phi' + \mathbf{Q}(x,\mu,\phi) \tag{2}$$

Here, $\mathbf{I}(x,\mu,\phi)$ is the Stokes vector expressed a function of the polar angle cosine μ (measured from the upward vertical), the azimuth angle ϕ relative to some fixed direction, and vertical optical thickness (for extinction) x measured from the top of the layer. ω is scattering albedo and $\mathbf{P}$ is the phase matrix for scattering of incident Stokes vectors with respect to the meridian plane.

At night, for the bottom layer ($x = \tau$, the total optical depth above the surface), $\mathbf{Q}$ has two terms:

$$\mathbf{Q}(\tau,\mu,\phi) = \frac{[1-\omega(\tau)]}{4\pi}\mathbf{B}(\tau) + \mathbf{R}(\tau,\mu,\phi) \tag{3}$$

where $\mathbf{B}$ denotes the emission that can be estimated by the Planck function expressed as a function of surface temperature, and $1-\omega(\tau)$ is effectively the surface absorptivity (also the emissivity according to Kirchhoff Law). Stokes vector $\mathbf{R}$ represents surface point or area sources of radiative emission that is not part of the surface emission. For most RTMs, there is no such term, and for this study, we use $\mathbf{R} = [R(0), 0, 0, 0]^T$. This input will then represent emissions by the fires and radiation from surface illumination sources (as described in the next paragraph and Eq. (5)). Both surface emissions and additional point or area emissions are regarded as unpolarized in our model. Since the angular distribution of **R** *at night* can vary with location (in the city and with different cities) and are not well characterized (and indeed largely unknown due to lack of observations), they are assumed to be isotropic (even though UNL-VRTM does consider the surface bi-directional distribution function or BRDF for daytime shortwave radiative transfer). This assumption is consistent with several past studies that have used VIIRS DNB to derive surface PM$_{2.5}$ and AOD at night (Zhang et al., 2008; Wang et al., 2016). Once the source term $\mathbf{Q}$ is modified to include additional emissions by fires and other illumination sources, the radiative transfer equation is then solved following standard discrete-ordinate methods (in which azimuth separation is conducted to obtain Fourier components).

As shown in Fig. 1b, the radiances emanating from a planar boundary (consisting of surface and buildings) as a result of illumination by the outdoor artificial lights can arise from two components. The first is the upward radiances emitted directly by outdoor bulbs, constituting the primary component of the upwelling surface light. A secondary component of upwelling light originates from downward artificial light emissions which are subsequently reflected upward. Both components are treated in our model, and the final leaving radiance from the surface and the bottom layer of the atmosphere as a result of surface illumination is the combination of these two components, which is given by

$$R(0) = I_{bulb}(1 + A_s) \tag{4}$$

where I_{bulb} is the radiance of the isotropic radiance from light bulb illumination, and A_s is the surface reflectance. With this implementation, UNL-VRTM is capable of considering light illumination over snow surfaces; the higher the surface reflectance, the larger the upwelling radiance (assuming other factors are equal). Depending on the nature of the illumination source, there are two ways to include it in the nighttime RTM. The first approach is the temperature-based light emission method, and the second is the bulb-type-based light emission method. Either way, the total upwelling radiance (from those emitted directly upward by the fires or light bulbs and those reflected by the surface) are considered as the surface-leaving radiance that is directly added as part of the source term in the equations describing the upward radiative transfer. It should be noted that only upwelling and downwelling signals are considered in this single-column RTM; horizontal propagation and related three-dimensional (3D) radiative transfer effects are neglected in the current version of the RTM. Given the non-columnated nature of most artificial light sources, the lack of account for 3D geometry represents one of the most significant sources of uncertainty in the model.

Planck function is used to account for fire radiative emission sources in the RTM. This is appropriate to calculate the light spectra of a system that obeys local thermodynamic equilibrium (LTE), such as wild fire and lava. Since the blackbody assumption in reality is invalid for either fire or lava, the new development further allows users to specify the wavelength-dependent emissivity that can be applied to the radiance intensity computed from the Planck's function. It is worth noting that estimation of visible light from Planck's function may have some uncertainties due to emission lines from potassium at 760 nm; however, such emission lines are also coincidently and partially overlap with oxygen absorption A band. In here, the basis for "blackbody" behavior from a fire flame is the incandescence of soot, basically a multiple-scattering regime resulting in absorptive heating of particles in the flame zone which radiate as blackbodies (Johnston et al., 2014). Johnston et al. (2014) further showed that flames >4 m deep are very close to black bodies in MWIR, and thinner flames are well-approximated by a 'grey body' treatment, which is to say that while they are not opaque, the light they emit matches the Planck curve. Hence, an emissivity term for fires is added as an option for users to account for the uncertainties from assuming fires as a blackbody.

Bulb-type light emissions from modern artificial lamps, such as LEDs, fluorescent lamps (FL), and high-pressure sodium lamps (HPS), do not follow Planck's function or Kirchhoff's Law. Here, we specify the intensity of light at each wavelength to create an emission spectrum for systems based either on theoretical analysis or laboratory measurements. Currently, we adopt lamp spectra datasets (Fig. 2) from the work of Elvidge et al. (2010) and implement them using a kernel-based method. In this method, our RTM is not only able to simulate the radiative transfer for a single lamp spectrum, but it also allows users to combine different lamp spectra in the dataset to generate a mixed (composite) spectrum for more complex scenarios, as shown in Eq. (5):

$$f_{composite}(\lambda) = \sum_{(i=1)}^{N} w_i f_{i,lamp}(\lambda),\ s.\ t.\ \begin{cases} \|f_{composite}\|_2 = C \\ \sum_{i=1}^{N} w_i = 1 \end{cases} \tag{5}$$

where $f_{i,\ lamp}$ is the ith kernel of the spectrum, w_i is the ith weight of that kernel, and C is the total power of the surface light emission. It can be useful for urban settings in which the light from the canopy surfaces is a mixture of different types of bulb emissions.

Since UNL-VRTM is a one-dimensional radiative transfer model, care must be taken with modeling the transfer of radiation from point sources in the instantaneous field of view (IFOV) by a satellite sensor. An inherent assumption of a plane-parallel atmosphere for UNL-VRTM also requires that for the IFOV of a particular pixel that contains point sources, the propagation of radiation from nearby pixels to this IFOV is neglected. This has been common practice in radiative transfer modeling applications for remote sensing of fires (see Matson and Dozier, 1981; Peterson and Wang, 2013, and references therein), and quantifying such uncertainties would require detailed field campaigns in future. However, within the same IFOV, the contribution of background radiation needs to be considered because the point sources may only occupy a fraction of the pixel area; therefore, we have added in UNL-VRTM the option to specify the area fraction of the point sources and the surface-leaving radiance intensity from the background. Then, the total upward radiance from the surface is the area-weighted sum of the radiances from the point sources and the background. Over cities, where the surface illumination can fill the entire VIIRS pixel area, the surface fraction for such illumination is effectively unity. This method again assumes that the emission from the background and the point sources are Lambertian, which is consistent with past work (Matson and Dozier, 1981; Peterson and Wang, 2013). Admittedly, the error of this assumption should be quantified in future studies with nocturnal field campaigns to characterize the angular distribution of surface illumination.

2.4. New development for DNB simulation

The RSR of the VIIRS DNB (e.g., Miller et al., 2013) is provided at 15 nm resolution by the VIIRS Characterization Support Team (VCST). Since the DNB measures radiance integrated across the range of 500–900 nm, it is important to consider the RSR in the simulation of DNB radiance. The RSR has been implemented in UNL-VRTM for the spectral convolution in the simulation of a panchromatic measurement of radiance as seen by VIIRS DNB. The implementation follows Eq. (6):

$$I_{VIIRS} = \int_{\lambda_1}^{\lambda_2} I_0(\lambda) t(\lambda) f_{RSR}(\lambda) d\lambda \tag{6}$$

where $I_0(\lambda)$ is the radiance of the surface emission at wavelength λ, and $t(\lambda)$ and $f_{RSR}(\lambda)$ are the atmospheric transmittance and VIIRS DNB RSR

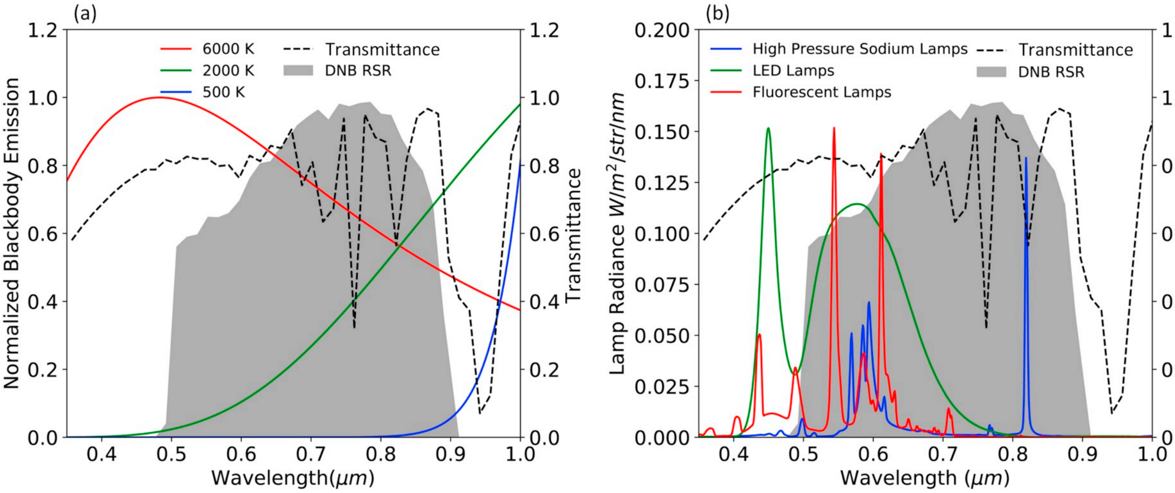

Fig. 2. (a) DNB RSR function (shaded grey area) and atmospheric transmittances (black dotted line for AOD = 0) overlaid with the blackbody emission spectra of fires for various temperature; (b) same as (a) but overlaid with the emission spectra of commonly used city lamps: (70-Watt) high pressure sodium lamp (HPS, blue line), standard (32-Watt) fluorescent tube (red line), and 100-Watt natural-white LED streetlight lamp (green line). (b) is adopted from Wang et al. (2016) with modification. (For interpretation of the references to color in this figure legend, the reader is referred to the web version of this article.)

at wavelength λ, respectively.

As shown in Fig. 2, the VIIRS DNB RSR covers a relatively wide spectrum range, over which atmospheric transmittance and surface light emission may vary considerably with wavelength, depending on the scenarios in question. The shape of DNB RSR itself is not uniform. It is shifted toward slightly longer wavelengths, which amplifies the impact of the longer wavelength radiance on the DNB measured radiance. Meanwhile, the radiance received by the DNB sensor is also affected by atmospheric processes (molecular scattering, gas absorption, aerosol scattering and absorption, etc.), which modify the atmospheric transmittance dramatically. In summary, DNB radiance is the result of the interaction among light sources, DNB RSR, and atmospheric factors. The impact of these factors on the DNB radiance, as well as on the retrieval of atmospheric parameters (e.g., AOD) will be carefully investigated in this study.

3. Model validation

3.1. Validation of the radiative transfer modeling of lunar light

We use the lunar radiance measured at Table Mountain in California, 26 June 2018 to evaluate the calculation of lunar light transfer in the atmosphere. This lunar radiance was measured by a spectrometer with a range from 617 nm to 675 nm and a resolution of 0.057 nm; the observation took place around 2 AM local time. There was also a co-located AERONET site, Table Mountain CA, measuring direct and diffuse solar light for inverting aerosol properties such as size parameters and the refractive index. Since there were no nighttime aerosol measurements at 2 AM, we apply the linear interpolation to the daytime aerosol measurements at 4 PM 25 June 2018 and 8 AM 26 June 2018 to obtain the desired nocturnal aerosol parameters at this time. Detailed information on the interpolated aerosol parameters from AERONET is illustrated in Table 1. The observed AOD on this day from AERONET is about 0.01 to 0.02 at 500 nm.

At 2 AM local time on 26 July 2018, the lunar zenith angle measured by the spectrometer was $\theta_{meas} = 31.31^{\circ}$, while the model simulated lunar zenith angle was $\theta_{simu} = 31.45^{\circ}$, which resulted in a relative bias of only 0.74% in the angle value. Since the spectrometer is pointed toward the moon, we set the relative azimuth angle in the simulation to 0°. The comparison of the simulated and the observed lunar radiance is shown in Fig. 3a. The shadowed area represents the ±25% uncertainty bar estimated for modeling. Sources of errors are: (1) the lunar irradiance database has an overall uncertainty of the order of 5%–10% (Miller and Turner, 2009); (2) the uncertainty of the interpolated AERONET AOD we use is around 0.01, which may ultimately result in a 10% radiance uncertainty; and (3) there are other potential factors that could cause uncertainties, such as the misrepresentation of the atmosphere profile in the model. As Fig. 3a illustrates, our simulation can capture the main absorption features and variance of the lunar radiance, for example, the H_2O absorption band near 657 nm show prominently.

Table 1
Atmospheric aerosol parameters of the Table Mountain in California, 26 June 2018.

Parameter	Value
Columnar fine mode volume	0.00384 ($\mu m^3/\mu m^2$)
Fine-mode effective radius (μm)	0.4675
Fine-mode effective variance (μm)	0.1530
Refractive index at 0.67 μm	1.54 − 0.029i
Columnar coarse mode volume	0.00577 ($\mu m^3/um^2$)
Coarse mode effective radius (μm)	2.424
Coarse mode effective variance (μm)	0.7453
Refractive index 0.67 μm	1.54 − 0.034i

3.2. Validation of the modeling of radiative transfer of surface light

Validation of RTM calculations for DNB over the artificial lights sources is unexpectedly challenging because it involves both DNB calibration and accuracy as well as accurate description of the surface light spectrum. Cao and Bai (2014) showed that DNB radiances from point sources at radiance levels as low as 3 nW cm^{-2} sr^{-1} can be measured by DNB; however, they found a difference of ~15% between DNB measurements and those simulated with the best knowledge of surface illumination (such as the power and bulb type) and atmospheric transmissivity.

Instead of making direct comparison between DNB measurements and forward RTM calculations based on optimal knowledge of surface illumination sources (total power and layout in a DNB pixel), DNB spatial spread response function, and atmospheric radiative properties, we conduct an indirect calibration of our model. The major assumption behind this approach is that the changes in the surface illumination of an isolated source within a two-week timeframe are small for days that have no snow at the surface. Hence, after atmospheric correction of DNB measurements of radiance at the TOA for a given isolated illumination source, the resultant surface-leaving radiances should be in much closer agreement (if not equal) to the counterpart DNB measurements without correction if the DNB measurements are taken with the same view geometry (e.g., 16 days apart, and that the moonlight source can be much smaller than the artificial light intensity).

With this calibration approach, we have chosen three AERONET ground stations in Beijing as validation locations for two days that have no snow on the ground and are within two weeks. VIIRS observations from two different days (one polluted day with high AOD of 0.8 and one clean day with low AOD of 0.2 at 440 nm; 0.502 and 0.138 at 0.675 nm) were chosen to implement the atmospheric correction required to obtain the aerosol-free VIIRS TOA radiance of each day (effectively the surface light intensity). After atmospheric correction, all the statistical indicators were improved (Fig. 3b). Root mean square error (RMSE) decreased from 0.08 to 0.04, and the bias decreased from 0.06 to 0.03. Moreover, the increase of the regression slope from 0.82 to 0.91 indicates the effectiveness of this atmospheric correction, which in turn indirectly validates our method of calculating the surface light transfer. Note, while AOD differs by a factor of 4 in these two days shown in Fig. 3b, the VIIRS DNB radiance only differs by a factor of 1.2. This disproportional contrast is in part due to: (a) the exponential decrease not linear decrease of radiance with respect of AOD from the surface to the space (e.g., following the Beer's law to yield radiance difference by a factor of 1.45), and (b) the larger single scattering albedo (0.96 at 675 nm) and larger particle size (0.61 μm in effective radius, and so, larger forward scattering) in the polluted day (as compared to the counterparts of 0.94 and 0.54 μm in the clean day). Indeed, the product of single scattering albedo and the phase function at the forward scattering of zero degree angle in clean day is ~93% of that in polluted day. Therefore, the radiances in the forward direction (as seen by VIIRS) is enhanced by the multiple scattering in the polluted days, explaining the relatively smaller difference of VIIRS DNB radiances in these two days.

3.3. Validation of Jacobian calculations

A special feature with linearized RTM such as UNL-VRTM is the capability to compute simultaneously the Stokes 4-vectors at TOA as well as their respective sensitivities (e.g., Jacobians or partial derivatives) to any set of parameters (hereafter, any parameters will be denoted by the symbol ξ) describing the aerosol scattering properties (such as single scattering albedo) and/or microphysical properties (such as index of refraction and size distribution). Such UNL-VRTM's capabilities for Jacobian calculations have been validated for the cases in which atmospheres and surfaces are illuminated by the Sun (Wang et al., 2014). Here, to evaluate the Jacobian capability for the nighttime

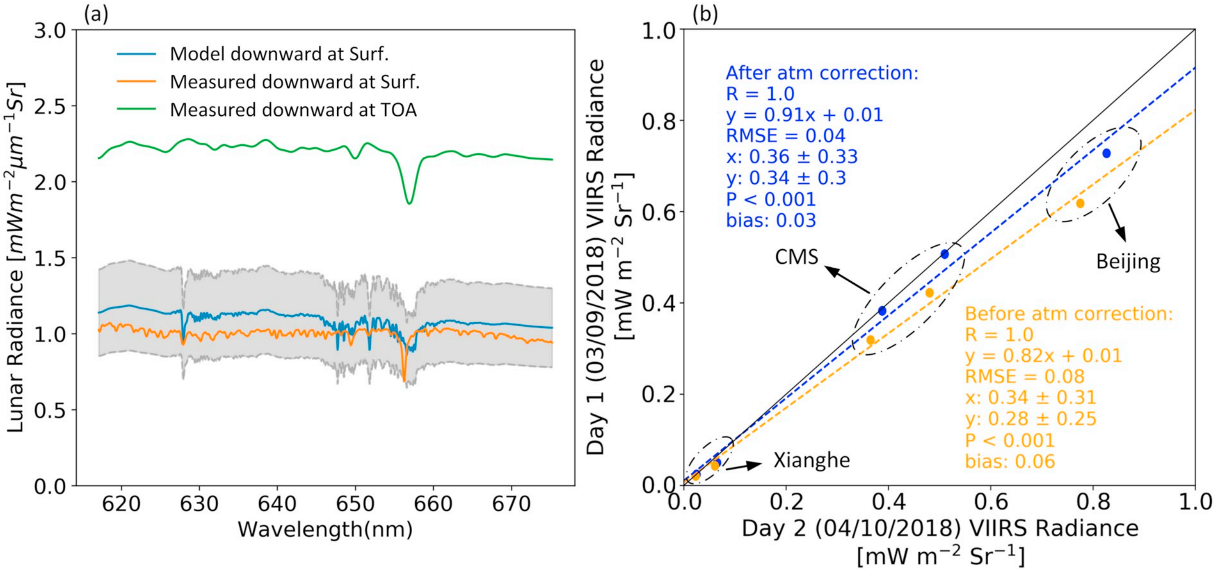

Fig. 3. (a) Comparison of the measured and simulated lunar radiance at the TOA and at the surface at Table Mountain Facility (TMF) of JPL. The shaded area represents the estimated uncertainty in the model simulation. (b) Inter-comparison between VIIRS DNB radiance between two days over three AERONET sites in Beijing area. Data before and after atmospheric correction are shown in blue and yellow respectively. For each AERONET sties whose station names are denoted in the figure, two DNB pixels that the site borders are respectively selected. The lower left two sets of points are radiances of the pixels closest to Xianghe AERONET site; the middle two and upper right two set of sites are closest to Beijing CMS AERONET and Beijing AERONET site, respectively. (For interpretation of the references to color in this figure legend, the reader is referred to the web version of this article.)

cases, we have carried out an inter-comparison of Jacobians calculated analytically from UNL-VRTM with their counterparts computed by Finite Differences (FD) method. The analytical calculation is the default option in UNL-VRTM, so that only one realization of UNL-VRTM is needed to compute the radiance and all appropriate Jacobians with respect to aerosol parameters ξ. In contrast, the FD method requires the realization of UNL-VRTM twice, one computation for the baseline case and another "perturbation" calculation in which the parameter of the interest is adjusted with a small finite difference. The resulting Stokes-vector differences between the two cases lead to the FD Jacobians. Obviously, the FD method is brute-force approach and should be avoided (if possible) because it is not only computationally inefficient, but can also lead to errors resulting from specific choices of the perturbation amounts.

Fig. 4 demonstrates the Jacobians of the Stokes-intensity with respect to AOD. Results from the analytical and the FD method are in excellent agreement on the 1:1 line. Since UNL-VRTM Jacobian calculations of Stokes' four parameters with respect to AOD and other aerosol and surface parameters in the conditions illuminated by the solar are already validated in Wang et al. (2014), the calculation results shown in Fig. 4 is made for the moonless nights and the illumination sources are from the surface only. The overall relative difference between the analytical Jacobians and DF-calculated counterparts is $<0.2\%$ for a wide range of AOD values from as low as 0.2 to as high as 0.8 over

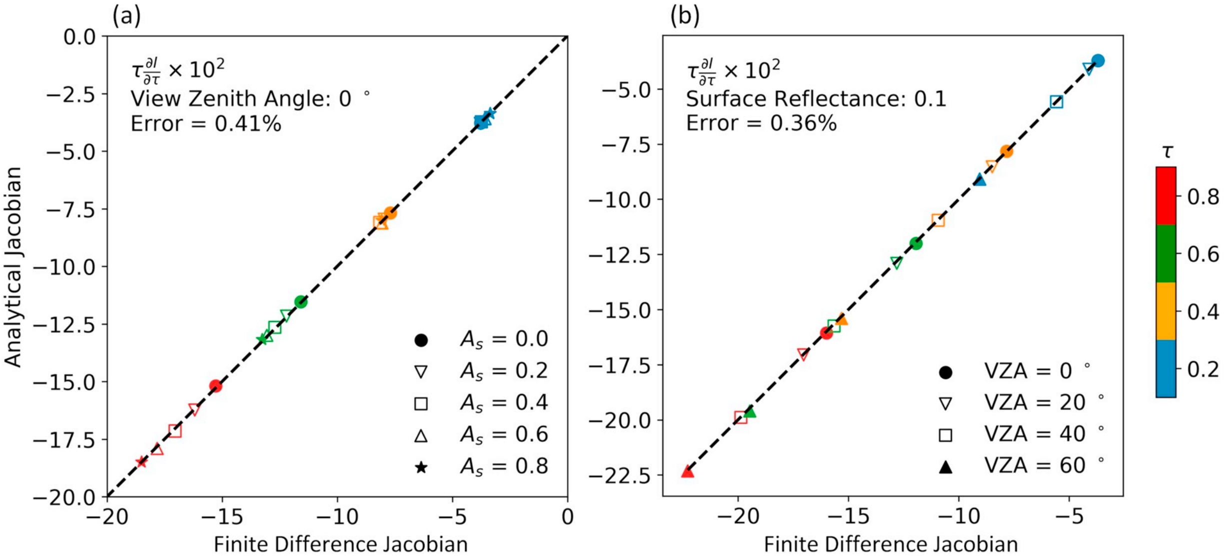

Fig. 4. Intercomparison of Jacobians ($\partial I/\partial \ln \tau$) calculated with UNL-VRTM using the analytical method (y-axis) with those computed from UNL-VRTM using finite difference estimates (x-axis) for moonless night illumiated by surface source only. (a) Jacobian of the TOA radiance with respect to AOD of different values of surface reflectance (A_s = 0, 0.2, 0.4, 0.6, 0.8). (b) Jacobian of the TOA radiance with respect to AOD of different values of view zenith angle (VZA = 0°, 20°, 40°, 60°). In both (a) and (b), results are shown for four AOD (τ) values of 0.2, 0.4, 0.6, and 0.8, respectively.

different surface reflectance with values of 0, 0.2, 0.6, and 0.8 (Fig. 4a) and different viewing geometries (Fig. 4b) with VZA values of 0°, 20°, 40°,and 60°. Clearly, all the Jacobian values are negative, suggesting the higher the AOD values, the smaller value is the intensity of upwelling radiance. For the low AOD values (0.2 or 0.4 shown as blue and yellow color symbols in the panel Fig. 4a), the Jacobians have similar values regardless of surface reflectance. As AOD increases (to 0.6 and 0.8), the Jacobians starts to show significant differences and becomes more negative for large surface reflectance (e.g., $As = 0.6$ or 0.8 shown as upper triangle and starts in Fig. 4a). This suggests that bright surfaces indeed favor the retrieval of large AOD at night from the illumination at the surface. The Jacobians also vary with viewing zenith angle (VZA) as shown in Fig. 4b. Overall, the Jacobians have more negative values for large VZA values and large AODs (e.g., squares and upper triangles of VZA of 40° and 60° in either blue or red colors for AOD of 0.6 or 0.8 are all shown in lower left corner of panel Fig. 4b). This can be understood because large VZA increases the path length for attenuating the surface light before it reaches sensor.

4. Application to VIIRS

To address specific questions related to VIIRS (especially DNB) as listed at the end of the Introduction section, we first define the normalized DNB radiance with respect to the surface illumination as the ratio of the TOA radiance and the surface radiance, representing the monochromatic atmospheric transmittance:

$$I_{norm} = \frac{\int_{\lambda_1}^{\lambda_2} I_0(\lambda)t(\lambda)f_{RSR}(\lambda)d\lambda}{\int_{\lambda_1}^{\lambda_2} I_0(\lambda)f_{RSR}(\lambda)d\lambda} \tag{7}$$

Conceptually, I_{norm} is useful to expediate the analysis, as it is related solely to the atmosphere effect; without such effect (transmittance term $t(\lambda) = 1$), $I_{norm} = 1$. Thus, the absolute power of surface illumination becomes irrelevant in this consideration, and this helps in our analysis to focus on the relative spectral variation of the surface illumination and atmospheric effects. In practice, for a VIIRS pixel of city light, assuming the total surface leaving radiance integrated over the hemisphere (e.g., a solid angle of 2π above the surface) yield a power of p (W m^{-2}), a scaling factor (S) can be computed for each typic light bulb or lamp types to obtain spectral surface radiance intensity (e.g., $I_0(\lambda)$) respectively for these bulb types (while still conserve p).

$$S = \frac{p}{2\pi\int_{\lambda_1}^{\lambda_2} I_{lamp}(\lambda)d\lambda} \tag{8}$$

$$I_0(\lambda) = S\ I_{lamp}(\lambda) \tag{9}$$

Three sets of sensitivity experiments (hereafter, Exp1, Exp2, and Exp3) for DNB have been designed; each experiment has one base case and one control case (and in all three cases, p is assumed to be 100 W m^{-2} although the actual value of p is irrelevant for analyzing I_{norm}). The base case is a realistic scenario with all factors included, while in the control case we change the factors of interest to test their impact. The specifics of these experiments are given in Table 2, with detailed descriptions provided in the following sub-sections. Results presented for each experiment are based on the aerosol optical properties used by Xu and Wang (2015) and tabulated in Table 3. The optical properties include particle size distribution and index of refraction for both fine and coarse model aerosols are based on the cluster analysis of the inversion data from AERONET sky light insensitive measurements. For the study here, we assume the fine-mode and coarse-mode particles have the same volume, which yields a fine-mode AOD fraction of 12% at 550 nm. Finally, a fourth experiment (Exp4) is performed to address specific questions related to fire measurements in the SWIR.

Table 2
Sensitivity experiments summary (see text for details).

	Exp. 1		Exp. 2		Exp. 3	
	Base	Control	Base	Control	Base	Control
RSR	√		√	√	√	
I_{uni}	√	√		√		
I_{lamp}			√		√	
$I_{\lambda 0}$						√

Table 3
Aerosol optical properties for fine and coarse mode used in the numerical experiments.[a]

Parameters	Coarse mode	Fine mode
Effective radius (μm)	2.337	0.162
Effective variance (μm)	0.495	0.299
Refraction index 0.67 μm	1.55 − 0.003i	1.44 − 0.011i
Single scattering albedo	0.834	0.937

[a] The data is based on the mean of multiple-year AERONET inversion data as in Xu and Wang (2015). For this study, the fine and coarse mode particles are assumed to have equal volume and the overall single scattering albedo is 0.925.

4.1. Exp1: impact of VIIRS RSR on AOD retrieval

First, to test how the effect of DNB RSR can affect the AOD retrieval, the base case has the DNB RSR taken into consideration; while in the control case, the DNB RSR is absent. Differences in DNB radiances between the two cases are investigated for a wide range of aerosol and surface conditions, and these differences are translated into the uncertainties in AOD retrievals through a look-up table approach. Uncertainties can be reported in both relative and absolute terms, as the true AOD is known in the forward simulation. Also, to focus directly on the question posed in this experiment, a wavelength independent or uniform surface spectrum (I_{uni}) has been assumed in this case.

The normalized DNB radiance with and without considering RSR for different view zenith angles (VZA) and AOD are shown in Fig. 5a and b, respectively. I_{norm} in the base case is larger than in the control case. This is because the slight shift of the RSR to the longer wavelengths suppresses the contribution of Rayleigh scattering (smaller at longer wavelengths), resulting in larger atmospheric transmittance. As expected, in Fig. 5c, the I_{norm} difference increases as the VZA increases for the same AOD. However, when the AOD is relatively low and the Rayleigh optical depth is relatively important, the I_{norm} is larger for large VZA (Fig. 5c).

By mapping the I_{norm} difference to AOD retrieval at 550 nm (which is chosen as the reference wavelength even though spectral AOD is considered in the radiative transfer calculation), the AOD retrieval bias caused by the RSR can be obtained. In this process, we treat the base case radiance as the true value, while the control case is used to construct the functional relationship between the radiance and AOD. This functional relationship is subsequently used to retrieve the AOD from the true (synthetic) radiance. For the same simplified cases, as in Fig. 5a and b, the AOD retrieval relative bias can be $>$100% for the conditions where AOD is less of 0.5; this is likely due to the fact that the interaction between the surface light and the atmospheric aerosol is weaker than that in the high AOD region (which ultimately is regulated by different wavelength dependences of scattering of aerosols and gas absorption), and hence the relative bias is high. With an increase of the AOD, the interaction between the surface and the aerosol is enhanced, and hence more accurate aerosol information can be extracted from the TOA radiance, which reduces the relative bias. In general, when AOD is relatively low ($<$0.5), the AOD retrieval bias can reach 100%. The retrieval bias decreases dramatically from ~50% to ~15% when AOD increases to 2. Our next experiment (Exp2) will extend our evaluation of the RSR effect by considering different light bulb spectra.

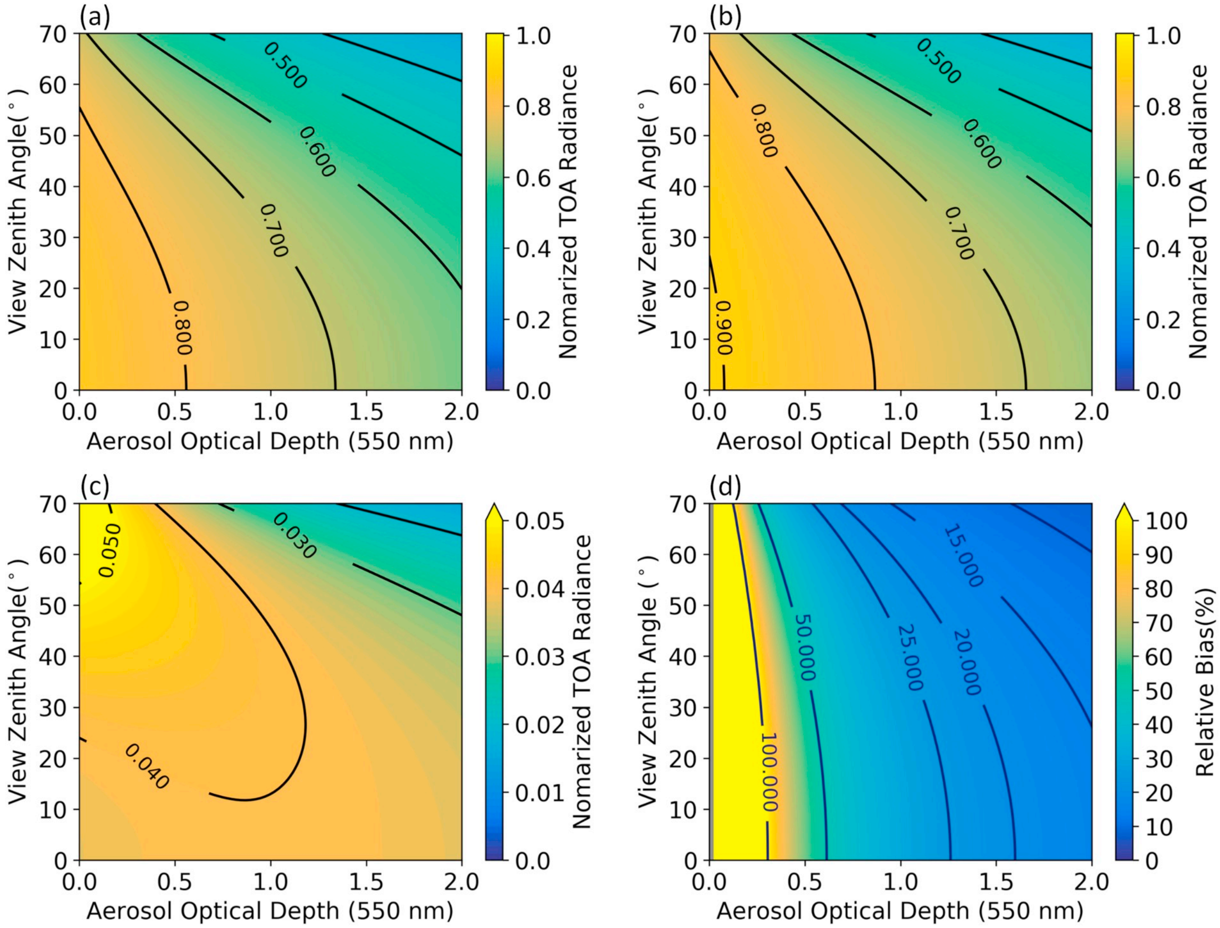

Fig. 5. Impacts of the RSR function on VIIRS DNB radiance simulation and AOD retrieval. (a) and (b) are normalized DNB radiance without and with DNB RSR considered, respectively. (c) shows the difference between (a) and (b), while (d) shows the relative AOD retrieval bias without DNB RSR considered.

4.2. Impacts of the surface spectrum on the AOD retrieval

As seen in Eq. (4), another important factor that regulates the DNB radiance is the Spectral Variation of Illumination (SVI) at the surface. In Fig. 2, for example, the spectrum of an HPS lamp (I_{lamp}) is mainly characterized by the sodium emission lines, centered at both 589 nm and 820 nm. In contrast, an FL lamp uses mercury vapor to produce shortwave ultraviolet light, then excites phosphor to glow. Its spectral range is from 400 to 700 nm, with several strong emission lines (430 nm, 480 nm, 550 nm, 580 nm, and 620 nm). Then again, an LED has a much smoother spectral shape, ranging from 400 to 800 nm, with a deep valley in the green band.

For the same overall electric power and energy efficiency, the SVI values for different bulb types can yield different TOA radiances, as the SVI for I_{lamp}convolves with the RSR of DNB, thereby affecting AOD retrievals. While a highly accurate SVI for each city light would not in general be available, it remains unclear the degree to which AOD retrieval uncertainty can arise from errors in SVI representation. Here, we conduct a nominal uncertainty analysis on this topic through theoretical means. In this experiment, the base case will consider both RSR and SVI for a specific type of bulb, while the control case will consider SVI as spectrally uniform (I_{uni}) or SVI for another artificial light source type.

To illustrate the approach, we show in Fig. 6 the values of I_{norm} for the base cases with LED, FL, and HPS lamps. I_{norm} values for LED and FL are similar because their respective SVIs are similar, yielding ~74% and 69% power in DNB, respectively. However, for HPS, ~90% of power is within the DNB spectral range, and its strong emission line at 820 nm is countermanded by the H_2O absorbing band, thereby reducing I_{norm} significantly.

Using the same concept as in Exp. 1, we can study how the SVI affects AOD retrieval when the SVI is considered spectrally invariant. We show in Fig. 6d through f that the AOD retrieval relative bias pattern is similar for LED and FL. The bias shifts from positive to negative as the AOD increases. This occurs for two reasons. First, the SVIs of LED and FL are mainly within the atmospheric window of 500–700 nm, while the wavelength-independent SVI will be affected by the strong H_2O absorption band in the 700–900 nm range. Thus, under the aerosol-free conditions, I_{norm} values from LED and FL are larger than those from a uniform SVI. Secondly, the Rayleigh optical depth within 500–700 nm is still large enough (0.14 decreasing to 0.04) to impact the light transfer. The I_{norm} values for LED and FL will be affected by both the aerosol and Rayleigh, while for the uniform SVI case, half of the spectra from 700 to 900 nm are nearly free from the impact of the Rayleigh scattering. Consequently, the decrease of I_{norm} is faster for LED and FL than for the uniform SVI case, as seen clearly in Fig. 7a. For the HPS, since a large part of its power is absorbed by the water vapor absorption band even in the aerosol-free conditions, I_{norm} is still smaller than for the wavelength-independent case (~10%); this results in a negative AOD retrieval relative bias. Overall, Fig. 6 reveals the importance of SVI to simulate DNB radiance for different surface reflectance and atmospheric conditions.

Quantitatively, for the same I_{norm} at TOA, the retrieved AOD may vary by up to 0.2 due to the different treatment of surface illumination types (Fig. 7a). For I_{norm} of 0.7, the AOD retrieved from using HPS spectra as illumination source is 0.25, while using LED, FL, and wavelength independent lamp spectra are 0.43, 0.42, and 0.45 respectively. Hence, retrieval of AOD over surface illuminated by HPS needs

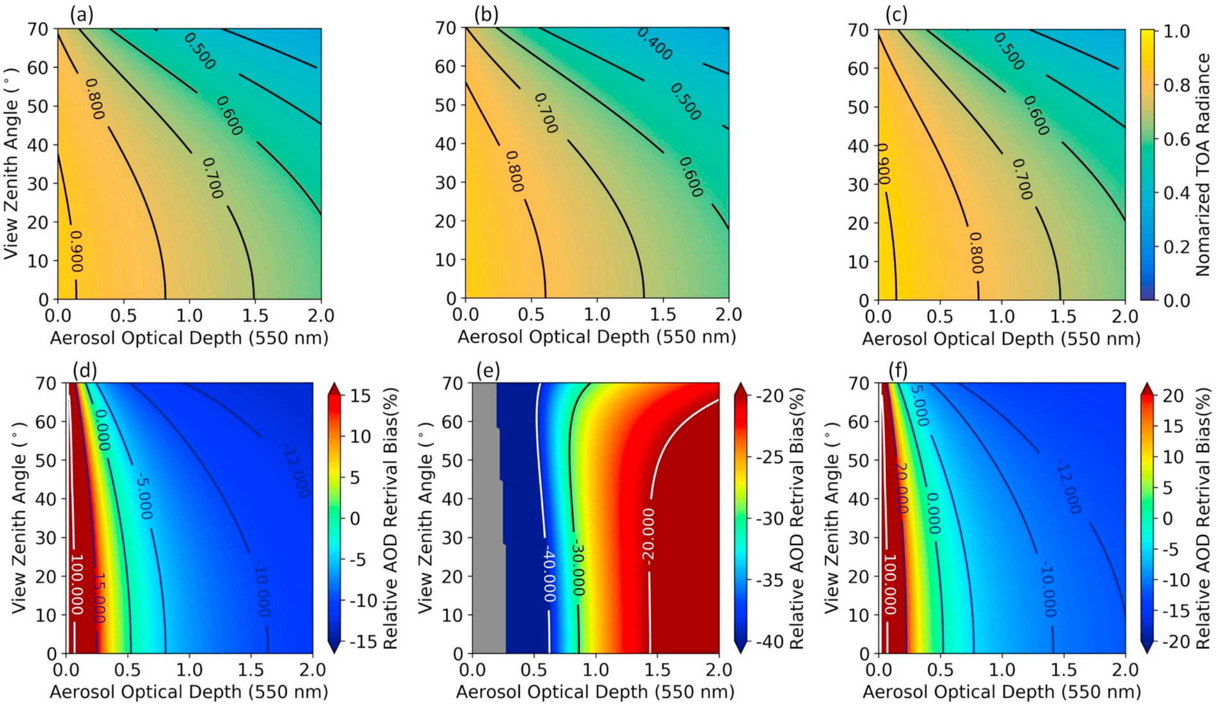

Fig. 6. (a)–(c) show I_{norm} for surfaces illuminated by LED, HPS, and FL bulbs, respectively, (d)–(f) show relative bias (in percentage) in AOD retrieval from (a)–(c) respectively if spectrally independent (or spectrally uniform) illumination spectra is used in the look-up table for AOD retrieval.

to pay special attention. The difference of AOD retrieval between using surface spectra of LED and FL lamp is small. Interestingly, for the same I_{norm} value of 0.7 for surface illuminated by HPS, if not considering Rayleigh scattering (e.g., only aerosol and gas absorption) in radiative transfer calculation, AOD retrieved would be 0.37, and if not considering gas absorption (e.g., only aerosol and Rayleigh), the retrieved AOD will be 0.79. This suggests that gas absorption can lead to ~0.52 difference in AOD (although such difference decreases as AOD increases) because HPS light spectra have overlaps with strong gas absorption lines of water vapor and O_2 A band, while Rayleigh can lead to difference of 0.11. In contrast, for the same I_{norm} value of 0.7 for surface illuminated by LED, if not considering Rayleigh scattering (e.g., only aerosol and gas absorption) in radiative transfer calculation, AOD retrieved would be 0.57, and if not considering gas absorption (e.g., only aerosol and Rayleigh), the retrieved AOD will be 0.66. Hence, Fig. 7c suggests that gas absorption can lead to ~0.23 difference in AOD (although such difference decreases as AOD increases), while Rayleigh scattering can lead to difference of 0.14.

4.3. Equivalent wavelength with respect to (w.r.t.) the AOD retrieval

As far as AOD retrieval is concerned, equivalent wavelength is defined as that wavelength at which the corresponding monochromatic radiance intensity can best represent the radiance intensity for a broadband as far as AOD retrieval is concerned. Since the polychromatic spectrum that DNB measures and effectively convolves with its RSR can be unknown, and also because the surface light source SVI is often unknown for a given DNB pixel, we hypothesize that an equivalent wavelength exists for AOD retrieval from DNB over surfaces that are illuminated by modern outdoor lights. If such a wavelength (within a band width of 5 nm) exists, a detailed consideration of spectral transmittance of the atmosphere in DNB can be largely simplified or ignored. In Exp. 3, we seek such an equivalent wavelength (λ_{equ}) through the following equation:

$$\lambda_{equ} = \underset{\lambda}{\arg}\ \min \sqrt{\frac{\sum_{i=1}^{N}(\tau_{retr}-\tau_{true})_i^2}{N}} \qquad (10)$$

where $T_{retr} = f_{\lambda i}^{-1}(I_{norm}(T_{true}))$, and $f_{\lambda i}^{-1}$ is the inverse function that links the narrow-band radiance at λ_i at TOA with τ and is prepared by pre-calculating through UNL-VRTM. Subscript i is the index for all wavelengths that will be evaluated, and it ranges from 1 to N, where N is the total number of possible wavelengths in the DNB to be considered. Eq. (10) is equivalent to finding a wavelength that has the least AOD retrieval RMSE for a series of true AOD values.

Fig. 8 shows the results of this exercise when a 5% retrieval error is selected as an acceptable threshold. In general, our calculations indicate that a wavelength around 585 nm is the commonest value of λ_{equ} for the three types of outdoor bulbs. However, for HPS, since there is a strong emission line in the NIR, a second equivalent wavelength exists near or slightly higher than 600 nm. Fig. 8 shows that the hypothesis is worthy of further evaluation for different scenarios of atmospheric, surface, and aerosol conditions.

4.4. AOD impact on DNB and SWIR for fire detection

For a given pixel area, the limit of fire detection depends on the background surface temperature, fire area, fire temperature, and atmospheric transmittance convolved with the sensor's RSR, as well as the convolution of the spatial layout of the fire distribution with the sensor point spread functions (Peterson and Wang, 2013; Peterson et al., 2013). To illustrate the application of the new developments in our model, we focus to study how the fire emissions of aerosols (i.e., smoke) may affect the detection; the latter topic has not been qualitatively studied in the literature. The smoke optical properties are taken from Wang and Christopher (2006), Xu et al. (2019), with mid-visible index of refraction of 1.5 – 0.012i and a log-normal size distribution with median radius 0.13 μm and geometric standard deviation of 0.44 μm. Fig. 9 shows DNB radiances (with treatment of mid-latitude summer atmospheric transmission and RSR) for different fire temperatures and area fractions without AOD. The background surface temperature is assumed to be 300 K. The black line represents a DNB radiance detection limit of 3 × 10^{-9} W cm^{-2} sr^{-1}. The figure shows that DNB is sensitive to flaming fire temperatures of >650 K for a fire fraction of 0.1 if AOD attenuation is not considered (Fig. 9a). However, if for the

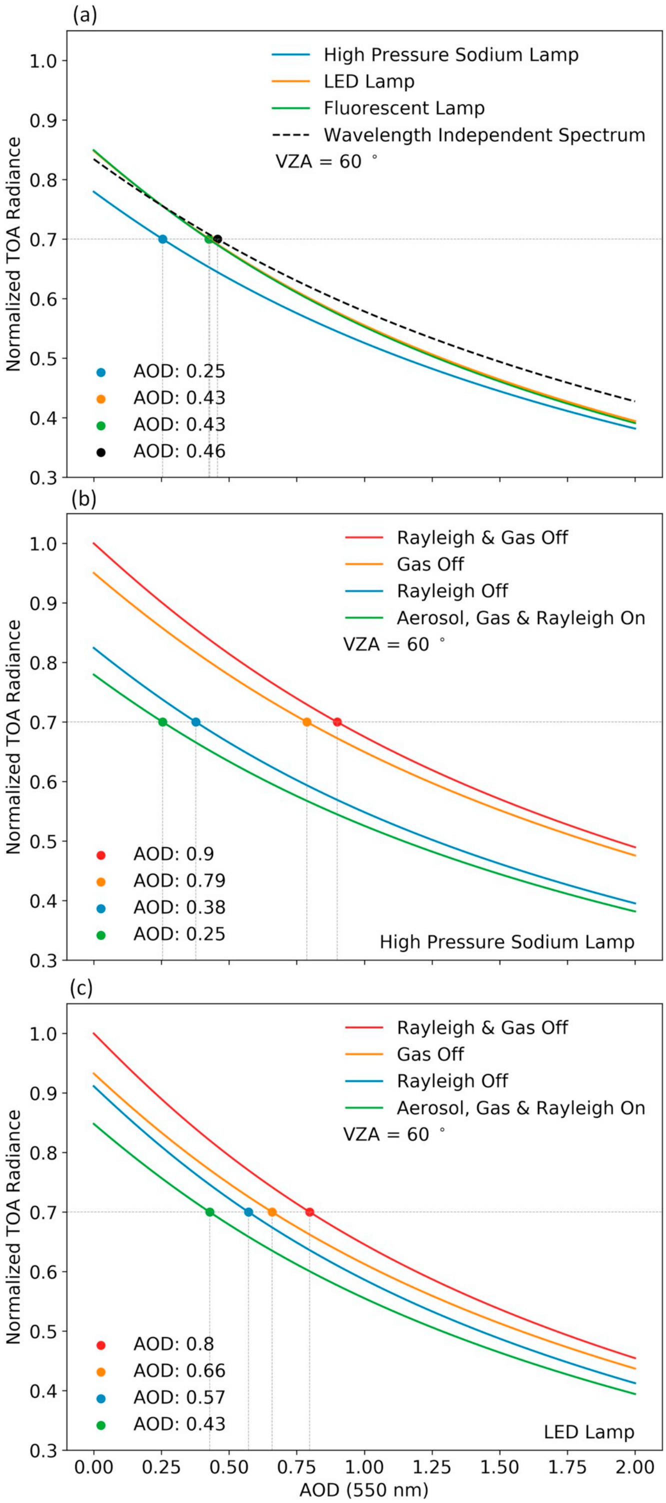

Fig. 7. (a) I_{norm} as a function of AOD for different surface illumination spectra. (b) and (c) are similar as (a) but respectively for surface illumination spectra of HPS only and LED only with different treatments of turning on and off gas absorption and Rayleigh scattering.

same flaming fire fraction of 0.1 and an AOD of 2.0, the DNB will be only sensitive to fires having temperatures larger than 700 K. In other words, when AOD is considered, the DNB detection limit for fires will be geared toward hotter or bigger fires (Fig. 9b).

Interestingly, the detection limit at 1.6 μm is 1.2 $\mathrm{Wm^{-2}\,sr^{-1}\,\mu m^{-1}}$. At this band, the variation of the sensitivity to fire detection appears to be similar to that for DNB. In other words, for a case with a fire fraction of 0.1, the 1.6-μm band can only detect fires that have temperatures larger than 650 K if the AOD effect is not considered and larger than 700 K when AOD values of 2 are considered. What is unexpected, however, is that the upper limit detection of 1.6 μm that saturates at 71.2 $\mathrm{Wm^{-2}\,sr^{-1}\,\mu m^{-1}}$ (Fig. 9c). Hence, for a fire fraction of 0.1, DNB can detect the fires with temperature up to 1050 K, and will be saturated for hotter fires. For fire area fraction of 0.00005 and AOD of 2.0, DNB can detect fires with temperature larger than 1000 K (as indicated by the black arrow in Fig. 9b), while 1.6 μm band can only sense the fires with temperature larger than 1500 K (as indicated by the black arrow in Fig. 9d). Since the 1.6 μm band is one of M-bands on VIIRS and its potential has been demonstrated by the past studies for detecting fires at night (Polivka et al., 2015), our result indicates that such detection with 1.6 μm band can have limitation for quantitatively characterizing hot and large fires, especially when not only the detection but also spectral fitting over this band and other TIR bands or quantitative calculation of FRP using band are conducted to retrieve fire area and temperature (Elvidge et al., 2013).

Finally, Fig. 9e and f show a zoom-in details in Fig. 9a and c respectively for the simulated DNB radiance and 1.6 μm radiance for the cases of fire area fraction <0.01. The contrast between Fig. 9e and f clearly demonstrates the higher sensitivity of DNB than 1.6 μm to detect smaller and cooler fires. For example, for fire area fraction of 0.002, DNB is capable to detect fires having temperature of 800 K while 1.6 μm band can only sense fires with temperature larger than 900 K.

4.5. *Jacobian analysis w.r.t. AOD and surface reflectance*

Fig. 10 further shows the relative sensitivity of TOA radiance to AOD $(\partial \ln I/\partial \ln \tau)$ as a function of surface reflectance and AOD itself. For the same surface reflectance, such sensitivity normally increases (more negative) as AOD increases regardless of the illumination bulb types (e.g., Fig. 10a–d corresponding to spectrally independent, LED, HPS, and FL respectively) and actual surface reflectance value; this is understood as the larger the AOD values, the higher reduction of radiance intensity during the transfer from surface to TOA, and thereby rendering higher signal to noise ratio for AOD retrievals. In addition, for the same surface reflectance, the rate of the relative sensitivity increases when AOD decreases, and for AOD larger than 1.5, further increase of AOD has much less effect on the relative sensitivity (e.g., the slope of isopleth of the relative sensitivity is close to zero when AOD is larger than 1.5).

In addition, Fig. 10 also reveals the advantage to retrieve AOD using surface illumination over visibly bright surfaces, which is in contrast of daytime AOD retrieval that often seeks to be dark over the dark surfaces. When AOD value is small, for the same AOD, the relative sensitivity of DNB intensity to AOD is nearly insensitive to the change of surface reflectance from dark to bright surfaces (e.g., slope of isopleth of the relative sensitivity is close to 0). However, as AOD increases to 0.6 and larger, the relative sensitivity increases (or more negative) as surface reflectance increases, suggesting a strength for retrieving AOD over bright (such as snow or ice) surfaces. This is understood that the higher the surface reflectance, for the same illumination by surface bulbs, the more surface-leaving radiances will interact with atmospheric particles before they reach the TOA, and the large signal for retrieving AOD. Hence, it is expected that if the reflectance of bright surfaces can be quantified, DNB nighttime remote sensing of AOD can be obtained with good accuracy, which can be used to supplement the passive remote sensing of AOD retrieval that are often at daytime.

5. Summary and discussions

In this paper, we have developed and added several key new elements in the UNL-VR TM in order to generate the nighttime radiative transfer modeling capability. Now, the tool can not only simulate

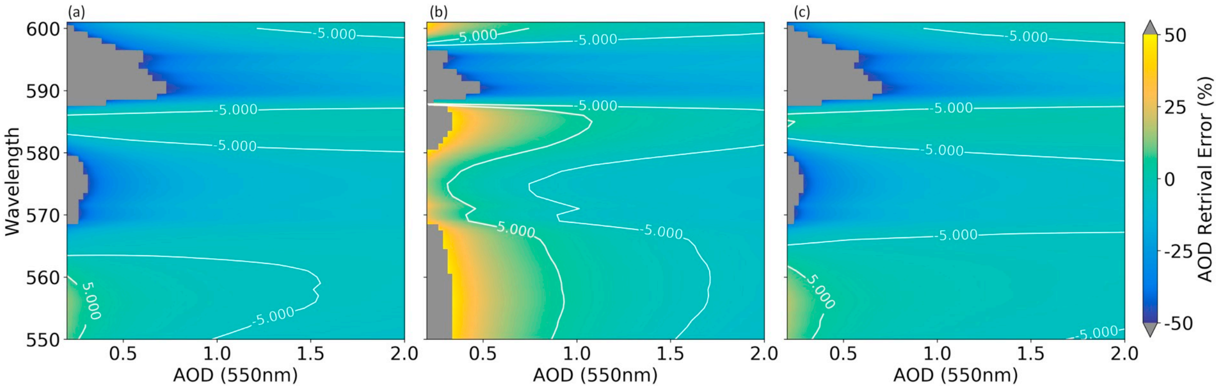

Fig. 8. Relative bias (in %) in AOD as a function of the true AOD (x-axis) and the narrow-band wavelengths (y-axis) used for the retrieval from DNB radiance for the surfaces illuminated by (a) LED, (b) HPS, and (c) FL, respectively. Regions with bias >50% is shown as grey.

backscattered radiation fields for nighttime scenarios illuminated by the Moon for at any given time and given location on Earth, it can also compute radiative transfer for any combination of surface artificial light sources of given temperature and spectrum shape. Cross validations were conducted to verify the correctness of the nighttime model implementations.

We have applied the nighttime radiative transfer model to the VIIRS DNB and addressed four key questions. First, when the DNB RSR, is omitted, the AOD bias can be greater than a 100% bias for values of AOD <0.5. This retrieval bias decreases as AOD increases. Second, AOD retrieval bias is spectrum-dependent. When a uniform (wavelength-independent) spectrum is assumed for the surface light source, the retrieved AOD bias is around –10% for LED and FL sources, but for HPS lamps, this bias is around –30%. This retrieval bias also decreases as the values of AOD rise. Third, the equivalent wavelength with respect to AOD retrieval for the chosen three lamp spectra is around 585 nm. Finally, as far as the detection of fires from VIIRS is concerned, the impact of AOD is more important for fire detection at 1.6 μm than in

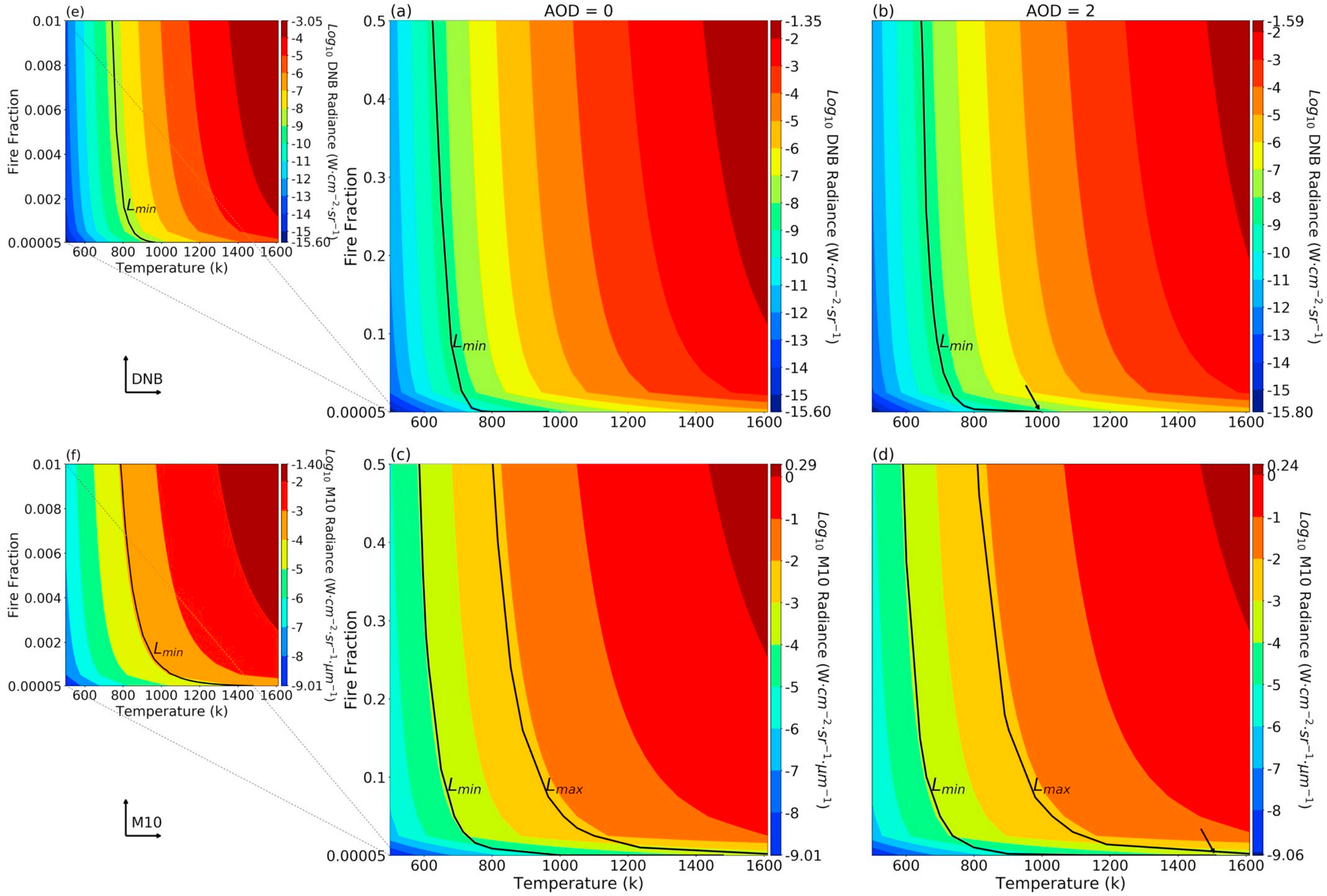

Fig. 9. (a) contour plot of simulated DNB radiance intensity for different fire temperatures (x-axis) and fire fractions (y-axis) during nighttime for mid-latitude atmospheric conditions without consideration of aerosol radiative effects (e.g., AOD = 0 in radiative transfer calculation); (b) is the same as (a) but with consideration of AOD of 2.0. The isopleth or contour line in black in (a) and (b) show the minimum radiance intensity that DNB sensor can detect, and the black arrow in (b) denotes the location where DNB minimum radiance intensity isopleth lines intersects with the x-axis (temperature). (c) and (d) are the same as (a) and (b) respectively but for 1.6-μm band. Panel (e) and (f) show the zoom-in details of the lower left portion of panel (a) and (c) respectively. See text for details.

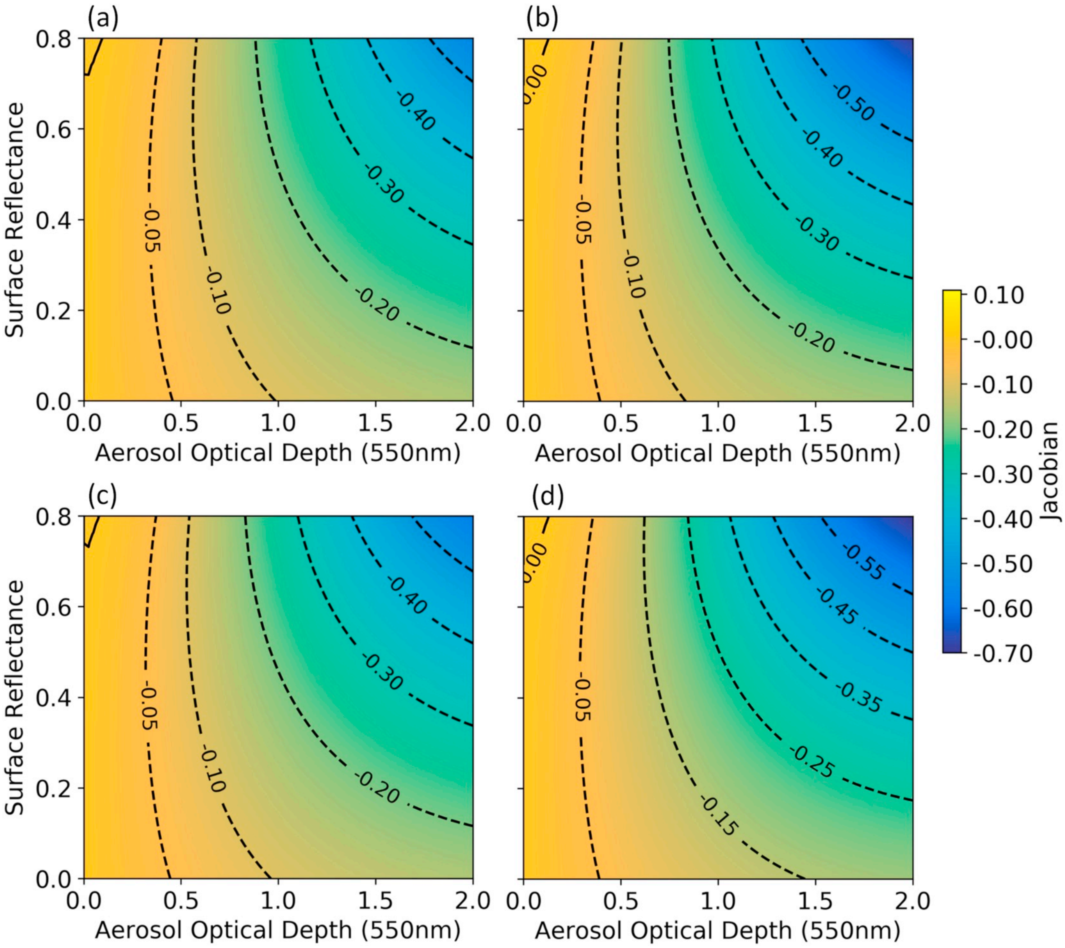

Fig. 10. Jacobians of TOA radiance with respect to AOD as a function of the true AOD (x-axis) and the reflectance (y-axis) of surface illuminated by (a) white bulb with spectrally uniform emission, (b) LED, (c) HPS, and (d) FL, respectively.

DNB because the 1.6 μm has a relatively lower detection limit for fires and is prone to saturation, and in the presence of smoke, it can only sense hotter and bigger fires (than what DNB can sense).

While the UNL-VRTM framework does consider azimuth dependence of light from point sources (as discussed in Section 2.3), it requires that such variation should be well characterized. Unfortunately, our current knowledge on the angular distribution of night-time visible light for VIIRS pixels over cities in only nascent (e.g.,Wang et al., 2016, Solbrig et al., 2020) at this time. As such, in our current modeling implementation, the light emanating from the pixel is simply assumed to be isotropic. This assumption is effectively the same as that made for existing 1D modeling infrared radiation. This is an approximation, but existing 3D RTMs, to our knowledge, have not been used in operational algorithms for remote sensing of fires and aerosols. Hence, our treatment of city lights as isotropic emission from the planar surface (e.g., the lowest level of UNL-VRTM) is also a compromise between 3D RTM theory and what can practically be provided to RTMs as observational inputs. With that said, the neglect of three-dimensional (3D) radiative transfer effects and the non-collimated nature of artificial light emission stand as large sources of uncertainty for 1D, plane-parallel radiative transfer calculations, and addressing these shortcomings is the focus of ongoing development for this model.

Author contributions section

J. W. conceived the idea of this paper. J.W., M.Z., X. Xu, and S. R. developed method and carried out the research. M.Z. and J.W. wrote the paper. S.M. provided moonlight model. S.M., J.R., E.H., and R.S. helped the writing. S. S. and T. P. provided surface moonlight data. All authors discussed the results and contributed to the final manuscript.

Declaration of competing interest

The authors declare that they have no known competing financial interests or personal relationships that could have appeared to influence the work reported in this paper.

Acknowledgement

This research was supported in part by NASA's Applied Sciences Program (grant number NNX14AG01G, managed by John A. Haynes), NASA's Terra/Aqua/S-NPP program (grant number 80NSSC18K0846 managed by Hal Maring), NASA's FIREX-AQ program (grant number 80NSSC18K0791 managed by Barry L. Lefer) and in part by Office of Naval Research (ONR's) Multidisciplinary University Research Initiatives (MURI) Program under the award N00014-16-1-2040.

References

Barreto, A., Cuevas, E., Damiri, B., Guirado, C., Berkoff, T., Berjón, A.J., Hernández, Y., Almansa, F., Gil, M., 2013. A new method for nocturnal aerosol measurements with a lunar photometer prototype. Atmos. Meas. Tech. 6 (3), 585–598.
Berk, A., Conforti, P., Kennett, R., Perkins, T., Hawes, F., Bosch, J., 2014. MODTRAN6: A major Upgrade of the MODTRAN Radiative Transfer Code. SPIE.
Bian, Y., Zhao, C., Xu, W., Ma, N., Tao, J., Kuang, Y., Zhao, G., Liu, H., 2017. Method to retrieve the nocturnal aerosol optical depth with a CCD laser aerosol detective system. Opt. Lett. 42 (22), 4607–4610.
Cao, C., Bai, Y., 2014. Quantitative analysis of VIIRS DNB nightlight point source for light

power estimation and stability monitoring. Remote Sens. 6 (12), 11915–11935.

Chen, X., Wang, J., Liu, Y., Xu, X., Cai, Z., Yang, D., Yan, C.-X., Feng, L., 2017. Angular dependence of aerosol information content in CAPI/TanSat observation over land: effect of polarization and synergy with A-train satellites. Remote Sens. Environ. 196, 163–177.

Chu, Y., Liu, Y., Li, X., Liu, Z., Lu, H., Lu, Y., et al., 2016. A review on predicting ground PM2.5 concentration using satellite aerosol optical depth. Atmosphere 7 (10).

Cinzano, P., Falchi, F., 2012. The propagation of light pollution in the atmosphere. Mon. Not. R. Astron. Soc. 427 (4), 3337–3357.

Croft, T.A., 1973. Burning waste gas in oil fields. Nature 245 (5425), 375–376.

Csiszar, I., Schroeder, W., Giglio, L., Ellicott, E., Vadrevu, K.P., Justice, C.O., Wind, B., 2013. Active fires from the Suomi NPP visible infrared imaging radiometer suite: product status and first evaluation results. J. Geophys. Res. Atmos. 119 (2), 85–96.

Ding, S., Wang, J., Xu, X., 2016. Polarimetric remote sensing in oxygen A and B bands: sensitivity study and information content analysis for vertical profile of aerosols. Atmospheric Measurement Techniques 9 (5), 2077–2092.

Dubovik, O., King, M., 2000. A flexible inversion algorithm for retrieval of aerosol optical properties from Sun and sky radiance measurements. J. Geophys. Res. Atmos. 105 (D16), 20673–20696.

Dubovik, O., Li, Z., Mishchenko, M.I., Tanré, D., Karol, Y., Bojkov, B., et al., 2019. Polarimetric remote sensing of atmospheric aerosols: instruments, methodologies, results, and perspectives. J. Quant. Spectrosc. Radiat. Transf. 224, 474–511.

Elvidge, C.D., Keith, D.M., Tuttle, B.T., Baugh, K.E., 2010. Spectral identification of lighting type and character. Sensors 10 (4), 3961.

Elvidge, C.D., Zhizhin, M., Hsu, F.-C., Baugh, K.E., 2013. VIIRS nightfire: satellite pyrometry at night. Remote Sens. 5 (9), 4423–4449.

Fu, D., Xia, X., Duan, M., Zhang, X., Li, X., Wang, J., Liu, J., 2018. Mapping nighttime PM2.5 from VIIRS DNB using a linear mixed-effect model. Atmos. Environ. 178, 214–222.

Gál, J., Horváth, G., Barta, A., Wehner, R., 2001. Polarization of the moonlit clear night sky measured by full-sky imaging polarimetry at full Moon: comparison of the polarization of moonlit and sunlit skies. J. Geophys. Res. 106 (D19), 22647–22653. https://doi.org/10.1029/2000JD000085.

Giglio, L., Descloitres, J., Justice, C.O., Kaufman, Y.J., 2003. An enhanced contextual fire detection algorithm for MODIS. Remote Sens. Environ. 87 (2–3), 273–282.

Giglio, L., Schroeder, W., Justice, C.O., 2016. The collection 6 MODIS active fire detection algorithm and fire products. Remote Sens. Environ. 178, 31–41.

Giles, D.M., Sinyuk, A., Sorokin, M.G., Schafer, J.S., Smirnov, A., Slutsker, I., et al., 2019. Advancements in the Aerosol Robotic Network (AERONET) version 3 database – automated near-real-time quality control algorithm with improved cloud screening for Sun photometer aerosol optical depth (AOD) measurements. Atmos. Meas. Tech. 12 (1), 169–209.

Hoff, R., Christopher, S.A., 2009. Remote sensing of particulate matter air pollution from space: have we reached the promised land? J. Air&Waste Manage. Assoc. 59, 642–675.

Hou, W., Wang, J., Xu, X., Reid, J.S., Han, D., 2016. An algorithm for hyperspectral remote sensing of aerosols: 1. Development of theoretical framework. J. Quant. Spectrosc. Radiat. Transf. 178, 400–415.

Hou, W., Wang, J., Xu, X., Reid, J.S., 2017. An algorithm for hyperspectral remote sensing of aerosols: 2. Information content analysis for aerosol parameters and principal components of surface spectra. J. Quant. Spectrosc. Radiat. Transf. 192, 14–29.

Ichoku, C., Ellison, L., 2014. Global top-down smoke-aerosol emissions estimation using satellite fire radiative power measurements. Atmos. Chem. Phys. 14 (13), 6643–6667.

Ichoku, C., Martins, J.V., Kaufman, Y.J., Wooster, M.J., Freeborn, P.H., Hao, W.M., Baker, S., Ryan, C.A., Nordgren, B.L., 2008. Laboratory investigation of fire radiative energy and smoke aerosol emissions. J. Geophys. Res. 113, D14S09. https://doi.org/10.1029/2007JD009659.

Johnson, R.S., Zhang, J., Hyer, E.J., Miller, S.D., Reid, J.S., 2013. Preliminary investigations toward nighttime aerosol optical depth retrievals from the VIIRS day/night band. Atmos. Meas. Tech. 6 (5), 1245–1255.

Johnston, J.M., Wooster, M.W., Lynham, T.W., 2014. Experimental confirmation of the MWIR and LWIR grey body assumption for vegetation fire flame emissivity. Int. J. Wildland Fire 23, 463–479.

Justice, C.O., Giglio, L., Korontzi, S., Owens, J., Morisette, J.T., Roy, D., Descloitres, J., Alleaume, S., Petitcolin, F., Kaufman, Y.J., 2002. The MODIS fire products. Remote Sens. Environ. 83 (83), 244–262.

Kaufman, Y.J., Kleidman, R.G., King, M.D., 1998a. SCAR-B fires in the tropics: properties and remote sensing from EOS-MODIS. J. Geophys. Res. 103, 31,955–931,986.

Kaufman, Y.J., Justice, C.O., Flynn, L.P., Kendall, J.D., Prins, E.M., Giglio, L., Ward, D.E., Menzel, W.P., Setzer, A.W., 1998b. Potential global fire monitoring from EOS-MODIS. J. Geophys. Res.-Atmos. 103 (D24), 32215–32238.

Kaufman, Y.J., Tanre, D., Boucher, O., 2002. A satellite view of aerosols in climate systems. Nature 419, 215–223.

King, M.D., Kaufman, Y.J., Tanre, D., Nakajima, T., 1999. Remote sensing of tropospheric aerosols from space: past, present, and future. Bull. Amer. Meteor. Soc. 80, 2229–2259.

Kokhanovsky, A.A., Leeuw, G., 2009. Satellite aerosol remote sensing over land. 388 pp. Springer-Science,, Praxis Publishing Ltd, Chichester, UK.

Kotchenova, S.Y., Vermote, E.F., 2007. Validation of a vector version of the 6S radiative transfer code for atmospheric correction of satellite data. Part II. Homogeneous Lambertian and anisotropic surfaces. Appl. Opt. 46 (20), 4455–4464.

Lee, T.E., Miller, S.D., Turk, F.J., Schueler, C.F., Julian, R., Deyo, S., Dills, P., Wang, S., 2006. The NPOESS/VIIRS day/night visible sensor. Bull. Amer. Meteor. Soc. 87 (2), 191–200. https://doi.org/10.1175/BAMS-87-2-191.

Lennartson, E., Wang, J., Castro Garcia, L., Ge, C., Carmichael, G., Gao, M., Kim, J., Janz, S., 2018. Diurnal variation of aerosol optical depth and PM2.5 in South Korea: a synthesis from AERONET, satellite (GOCI), KORUS-AQ observation, and WRF-Chem model. Atmos. Chem. Phys. Discuss. 2018, 1–32.

Li, Z., Li, K., Li, D., Yang, J., Xu, H., Goloub, P., Victori, S., 2016. Simple transfer calibration method for a Cimel Sun–Moon photometer: calculating lunar calibration coefficients from Sun calibration constants. Appl. Opt. 55 (27), 7624–7630.

Liu, Q., Boukabara, S., 2014. Community Radiative Transfer Model (CRTM) applications in supporting the Suomi National Polar-orbiting Partnership (SNPP) mission validation and verification. Remote Sens. Environ. 140, 744–754.

Matson, M., Dozier, J., 1981. Identification of subresolution high-temperature sources using a thermal Ir sensor. Photogramm. Eng. Remote Sens. 47 (9), 1311–1318.

McHardy, T.M., Zhang, J., Reid, J.S., Miller, S.D., Hyer, E.J., Kuehn, R.E., 2015. An improved method for retrieving nighttime aerosol optical thickness from the VIIRS day/night band. Atmos. Meas. Tech. 8 (11), 4773–4783.

Miller, S.D., Turner, R.E., 2009. A dynamic lunar spectral irradiance data set for NPOESS/VIIRS day/night band nighttime environmental applications. IEEE Trans. Geosci. Remote Sens. 47 (7), 2316–2329.

Miller, S.D., Mills, S.P., Elvidge, C.D., Lindsey, D.T., Lee, T.F., Hawkins, J.D., 2012. Suomi satellite brings to light a unique frontier of environmental imaging capabilities. Proc. Natl. Acad. Sci. 109 (39), 15706–15711.

Miller, S.D., Straka, W., Mills, S., Elvidge, C., Lee, T., Solbrig, J., Walther, A., Heidinger, A., Weiss, S., 2013. Illuminating the capabilities of the Suomi National Polar-Orbiting Partnership (NPP) Visible Infrared Imaging Radiometer Suite (VIIRS) day/night band. Remote Sens. 5 (12), 6717.

Miller, S.D., Straka, W.C., Yue, J., Smith, S.M., Alexander, M.J., Hoffmann, L., Setvák, M., Partain, P.T., 2015. Upper atmospheric gravity wave details revealed in night glow satellite imagery. Proc. Natl. Acad. Sci. 112 (49), 6728–6735. https://doi.org/10.1073/pnas.1508084112.

Pellicori, S., 1971. Polarizing properties of pulverized materials with special reference to the lunar surface. Appl. Opt. 10, 270–285.

Peterson, D., Wang, J., 2013. A sub-pixel-based calculation of fire radiative power from MODIS observations: 2. Sensitivity analysis and potential fire weather application. Remote Sens. Environ. 129, 231–249.

Peterson, D.A., Wang, J., Ichoku, C., Hyer, E., Ambrosia, V., 2013. A sub-pixel-based calculation of fire radiative power from MODIS observations: 1: algorithm development and initial assessment. Remote Sens. Environ. 129 (0), 262–279.

Peterson, D.A., Hyer, E., Wang, J., 2014. Quantifying the potential for high-altitude smoke injection in the North American boreal forest using the standard MODIS fire products and subpixel-based methods. J. Geophys. Res. Atmos. 119 (6), 2013JD021067.

Petrenko, M., Kahn, R., Chin, M., Soja, A., Kucsera, T., Harshvardhan, 2012. The use of satellite-measured aerosol optical depth to constrain biomass burning emissions source strength in the global model GOCART. J. Geophys. Res. Atmos. 117 (D18), D18212.

Polivka, T., Hyer, E., Wang, J., Peterson, D., 2015. First global analysis of saturation artifacts in the VIIRS infrared channels and the effects of sample aggregation. IEEE Geosci. Remote Sens. Lett. 1262–1266, 2015.

Polivka, T.N., Wang, J., Ellison, L.T., Hyer, E.J., Ichoku, C.M., 2016. Improving nocturnal fire detection with the VIIRS day-night band. IEEE Trans. Geosci. Remote Sens. 54 (9), 5503–5519.

Prins, E.M., Feltz, J.M., Menzel, W.P., Ward, D.E., 1998. An overview of GOES-8 diurnal fire and smoke results for SCAR-B and 1995 fire season in South America. J. Geophys. Res.-Atmos. 103 (D24), 31821–31835.

Ricchiazzi, P., Yang, S., Gautier, C., Sowle, D., 1998. SBDART: a research and teaching software tool for plane-parallel radiative transfer in the Earth's atmosphere. Bull. Am. Meteorl. Soc. 79, 2101–2114.

Rodgers, C.D., 2000. Inverse Methods for Atmospheric Sounding: Theory and Practice. World Sci., Hackensack, N. J.

Schlyter, P., 2010. Computing Planetary Positions-A Tutorial With Worked Examples. (Downloaded March, 26, 2010).

Schroeder, W., Oliva, P., Giglio, L., Csiszar, I.A., 2014. The new VIIRS 375m active fire detection data product: algorithm description and initial assessment. Remote Sens. Environ. 143, 85–96.

Solbrig, J.E., Miller, S.D., Zhang, J., Grasso, L.D., Kliewer, A., 2020. Assessing the stability of surface lights for use in retrievals of nocturnal atmospheric parameters. Atmos. Meas. Tech. https://doi.org/10.5194/amt-2019-103. (press).

Spurr, R.J.D., 2006. VLIDORT: a linearized pseudo-spherical vector discrete ordinate radiative transfer code for forward model and retrieval studies in multilayer multiple scattering media. J. Quant. Spectrosc. Radiat. Transf. 102 (2), 316–342. https://doi.org/10.1016/j.jqsrt.2006.05.005.

Spurr, R.J.D., Christi, M., 2019. The LIDORT and VLIDORT linearized scalar and vector discrete ordinate radiative transfer models: an update for the last 10 years. Light Scattering Reviews 12, 1–62 (ed. A. Kokhanovsky, Springer).

Spurr, R., Wang, J., Zeng, J., Mishchenko, M., 2012. Linearized T-matrix and Mie scattering computations. J. Quant. Spectrosc. Radiat. Transf. 113, 425–439.

van Donkelaar, A., Martin, R.V., Spurr, R.J.D., Drury, E., Remer, L.A., Levy, R.C., Wang, J., 2013. Optimal estimation for global ground-level fine particulate matter concentrations. J. Geophys. Res. Atmos. 118 (11), 5621–5636.

Wang, J., Christopher, S.A., 2003. Intercomparison between satellite-derived aerosol optical thickness and PM2.5 mass: implications for air quality studies. Geophys. Res. Lett. 30 (21), 2095 (doi:2010.1029/2003GL018174).

Wang, J., Christopher, S.A., 2006. Mesoscale modeling of Central American smoke transport to the United States: 2. Smoke radiative impact on regional surface energy budget and boundary layer evolution. J. Geophys. Res. Atmos. 111 (D14), D14S92.

Wang, J., Xu, X., Ding, S., Zeng, J., Spurr, R., Liu, X., Chance, K., Mishchenko, M., 2014. A numerical testbed for remote sensing of aerosols, and its demonstration for evaluating retrieval synergy from a geostationary satellite constellation of GEO-CAPE and

GOES-R. J. Quant. Spectrosc. Radiat. Transf. 146 (0), 510–528.

Wang, J., Aegerter, C., Xu, X., Szykman, J.J., 2016. Potential application of VIIRS day/night band for monitoring nighttime surface PM2.5 air quality from space. Atmos. Environ. 124, 55–63.

Wang, J., Roudini, S., Hyer, E., Zhou, M., Castro Garcia, L., Reid, J., Peterson, D., Da Silva, A., 2020. Detecting nighttime fire combustion phase by hybrid application of visible and infrared radiation from Suomi NPP VIIRS. Remote Sens. Environ. 237, 111466. https://doi.org/10.1016/j.rse.2019.111466.

Wang, Y., Wang, J., Levy, R.C., Xu, X., Reid, J.S., 2017. MODIS retrieval of aerosol optical depth over turbid coastal water. Remote Sens. 9 (6), 595.

Wolfe, R.E., Lin, G., Nishihama, M., Tewari, K.P., Tilton, J.C., Isaacman, A.R., 2013. Suomi NPP VIIRS prelaunch and on-orbit geometric calibration and characterization. J. Geophys. Res. Atmos. 118 (20).

Xu, X., Wang, J., 2015. Retrieval of aerosol microphysical properties from AERONET photo-polarimetric measurements: 1. Information content analysis. J. Geophys. Res. Atmos. 120 (14), 7059–7078.

Xu, X., Wang, J., Zeng, J., Spurr, R., Liu, X., Dubovik, O., et al., 2015. Retrieval of aerosol microphysical properties from AERONET photopolarimetric measurements: 2. A new research algorithm and case demonstration. J. Geophys. Res.-Atmos. 120 (14), 7079–7098.

Xu, X., Wang, J., 2015. Retrieval of aerosol microphysical properties from AERONET photopolarimetric measurements: 1. Information content analysis. J. Geophys. Res 120 (14), 7059–7078. https://doi.org/10.1002/2015JD023113.

Xu, X., Wang, J., Wang, Y., Zeng, J., Torres, O., Yang, Y., Marshak, A., Reid, J., Miller, S., 2017. Passive remote sensing of altitude and optical depth of dust plumes using the oxygen A and B bands: first results from EPIC/DSCOVR at Lagrange-1 point. Geophys. Res. Lett. 44 (14), 7544–7554.

Xu, X., Wang, J., Zeng, J., Hou, W., Meyer, K.G., Platnick, S.E., Wilcox, E.M., 2018. A pilot study of shortwave spectral fingerprints of smoke aerosols above liquid clouds. J. Quant. Spectrosc. Radiat. Transf. 221, 38–50.

Zhang, J., Reid, J.S., Miller, S.D., Turk, F.J., 2008. Strategy for studying nocturnal aerosol optical depth using artificial lights. Int. J. Remote Sens. 29 (16), 4599–4613.

Xu, X., Wang, J., Zeng, J., Torres, O., Reid, J.S., Miller, S.D., Martins, J.V., Remer, L.A., 2019. Detecting layer height of smoke aerosols over vegetated land and water surfaces via oxygen absorption bands: Hourly results from EPIC/DSCOVR satellite in deep space. Atmos. Meas. Tech. 12 (6), 3269–3288. https://doi.org/10.5194/amt-12-3269-2019.

Zhang, J., Jaker, S.L., Reid, J.S., Miller, S.D., Solbrig, J., Toth, T.D., 2018. Characterization and application of artificial light sources for nighttime aerosol optical depth retrievals using the VIIRS day/night band. Atmos. Meas. Tech. Discuss. 2018, 1–45.